Inferring the Focal Depths of Small Earthquakes in Southern California Using Physics-Based **Waveform Features**

Keith D. Koper*¹, Relu Burlacu¹, Riley Murray¹, Ben Baker¹, Rigobert Tibi², and Abdullah Mueen³

ABSTRACT

Determining the depths of small crustal earthquakes is challenging in many regions of the world, because most seismic networks are too sparse to resolve trade-offs between depth and origin time with conventional arrival-time methods. Precise and accurate depth estimation is important, because it can help seismologists discriminate between earthquakes and explosions, which is relevant to monitoring nuclear test ban treaties and producing earthquake catalogs that are uncontaminated by mining blasts. Here, we examine the depth sensitivity of several physics-based waveform features for ~8000 earthquakes in southern California that have well-resolved depths from arrival-time inversion. We focus on small earthquakes ($2 < M_L < 4$) recorded at local distances (< 150 km), for which depth estimation is especially challenging. We find that differential magnitudes (M_w/M_L-M_c) are positively correlated with focal depth, implying that coda wave excitation decreases with focal depth. We analyze a simple proxy for relative frequency content, $\Phi \equiv \log_{10} (M_0) + 3 \log_{10} (f_c)$, and find that source spectra are preferentially enriched in high frequencies, or "blue-shifted," as focal depth increases. We also find that two spectral amplitude ratios Rg 0.5-2 Hz/Sg 0.5-8 Hz and Pg/Sg at 3-8 Hz decrease as focal depth increases. Using multilinear regression with these features as predictor variables, we develop models that can explain 11%-59% of the variance in depths within 10 subregions and 25% of the depth variance across southern California as a whole. We suggest that incorporating these features into a machine learning workflow could help resolve focal depths in regions that are poorly instrumented and lack large databases of well-located events. Some of the waveform features we evaluate in this study have previously been used as source discriminants, and our results imply that their effectiveness in discrimination is partially because explosions generally occur at shallower depths than earthquakes.

KEY POINTS

- Inferring the depths of small seismic events is important for source discrimination and seismic monitoring.
- We analyzed waveforms from ~8000 well-located southern California events to find depth-sensitive features.
- Increased focal depth correlates with decreased coda waves, increased frequency content, and decreased P/S ratios.

Supplemental Material

INTRODUCTION

Discriminating underground nuclear explosions from earthquakes is a longstanding problem in observational seismology (Douglas, 2013). Many methods exist for source discrimination of moderate-to-large seismic events (M > 3.5-4.0) that are well recorded at regional-to-teleseismic distances (>300 km; (e.g., Richards and Zavales, 1990; Bowers and Selby, 2009). However, source discrimination of small seismic events that are well recorded only at local-to-regional distances remains challenging (e.g., National Research Council, Policy and Global Affairs, and Committee on Reviewing and Updating Technical Issues Related to the Comprehensive Nuclear Test Ban Treaty, 2012; Maceira et al., 2017). This problem is relevant to society and policy makers, because the Comprehensive

Cite this article as Koper, K. D., R. Burlacu, R. Murray, B. Baker, R. Tibi, and A. Mueen (2024). Inferring the Focal Depths of Small Earthquakes in Southern California Using Physics-Based Waveform Features, Bull. Seismol. Soc. Am. XX, 1-21, doi: 10.1785/0120230307

© Seismological Society of America

^{1.} Department of Geology and Geophysics, University of Utah, Salt Lake City, Utah, U.S.A., (b) https://orcid.org/0000-0002-9725-6509 (KDK); (b) https://orcid.org/0000-National Laboratories, Albuquerque, New Mexico, U.S.A., https://orcid.org/0000-0002-4784-3940 (RT); 3. Department of Computer Science, University of New Mexico, Albuquerque, New Mexico, U.S.A.

^{*}Corresponding author: koper@seis.utah.edu

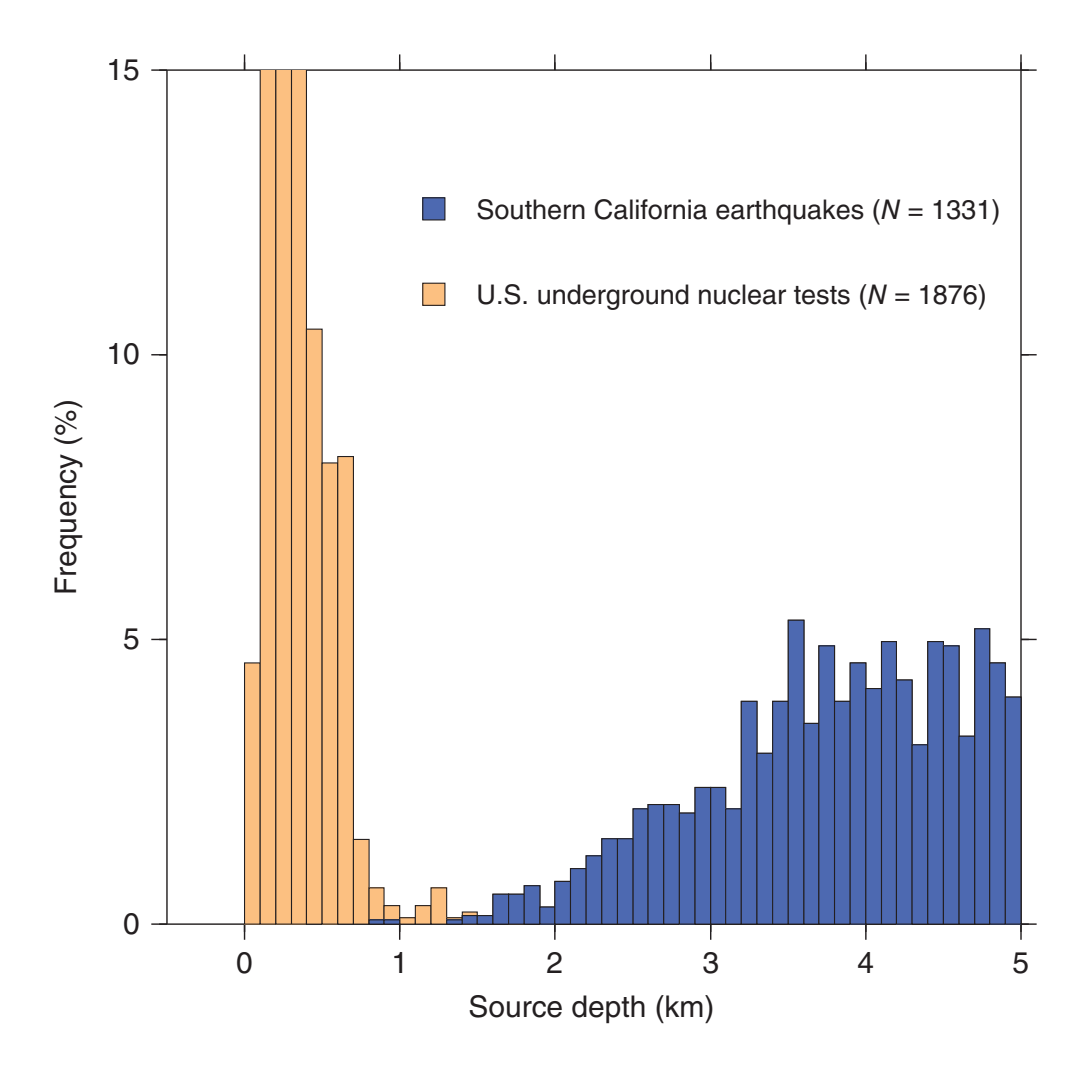


Figure 1. Comparison of source depths for all underground U.S. nuclear tests (U.S. Department of Energy, 2015) and small (2 < M < 4) southern California earthquakes during 1 January 2001–31 December 2019 (Hauksson *et al.*, 2012) with especially well-constrained hypocenters as described in Siddiquee *et al.* (2022). In both the cases, depth is relative to Earth's surface. The *y* axis is purposely saturated at 15% to improve the presentation.

Nuclear Test Ban Treaty is a zero-tolerance agreement that prohibits all nuclear tests, no matter how small. Discrimination of small seismic sources is also relevant to regional seismic network operators who aim to generate earthquake catalogs that are free from mine blasts and other types of chemical explosions (e.g., Koper, 2019). Earthquake catalogs that are contaminated by explosions can result in incorrect magnitude–frequency relationships and thus biased estimates of seismic hazard (e.g., Horasan *et al.*, 2009; Gulia and Gasperini, 2021).

An important tool in seismic source discrimination is the accurate and precise estimation of focal depth. Seismic sources that occur greater than ~2–3 km beneath Earth's surface can reliably be inferred to be earthquakes and screened out as potential explosions (Fig. 1). For earthquakes larger than about M 3.5, depth is often well constrained via moment tensor inversion of regional waveforms (e.g., Dreger and Helmberger, 1993; Herrmann *et al.*, 2011). For smaller events, the lack of accurate high-frequency Green's functions limits the applicability of

waveform inversion, although sometimes forward modeling approaches can be used (e.g., Ma et al., 2010; He et al., 2019; Yuan, et al., 2020). Source depth can be well constrained by first-arriving *P* and *S* waves during event location, but only for areas with dense seismic instrumentation in which the nearest station is within ~1.0 to 1.5 focal depths of an earthquake (Gomberg et al., 1990). For most regions of the Earth, the depths of small seismic events are relatively poorly constrained, presenting a challenge for source discrimination.

Recently, a machine learning model (Septor) was trained to infer the depths of small earthquakes (2 < M < 4) in southern California using seismic data recorded at distances mostly less than 120 km (Siddiquee et al., 2022). Southern California has a high density of seismometers, ensuring that many earthquake depths are well resolved during routine location, and a large set of high-quality depth labels is available for training purposes. Septor consists of a waveform aggregator and a station aggregator. The waveform

aggregator is a convolutional neural network (CNN)-long-short term memory (LSTM) model than operates on a three-component scalogram from a single station and produces a 2D array of features. The station aggregator is a second CNN-LSTM model that operates on feature arrays from the nearest five stations to an earthquake and outputs source depth. Having trained *Septor* with data from 7524 earthquakes, Siddiquee *et al.* (2022) found a correlation coefficient of 0.701 between *Septor*-predicted depths and observed depths for a "hold-out" group of 835 earthquakes.

Septor uses source–receiver distance information in its station aggregator and is designed to be used after an initial epicenter has been determined. In the context of seismic monitoring, it would be useful if Septor could be applied to infer the depths of small seismic events in other data-poor regions where source depths are not well constrained by arrival times but epicentral information exists. A difficulty with this approach is that deep learning models sometimes do not generalize to datasets that are markedly different from their

training data. For example, Siddiquee *et al.* (2022) found that when the southern California trained *Septor* was applied to data from 1777 earthquakes in northern California, the correlation coefficient between predicted and observed depths dropped to 0.153. Presumably, *Septor* had learned details about the geological structure of southern California (i.e., path and site effects) that did not translate well to northern California.

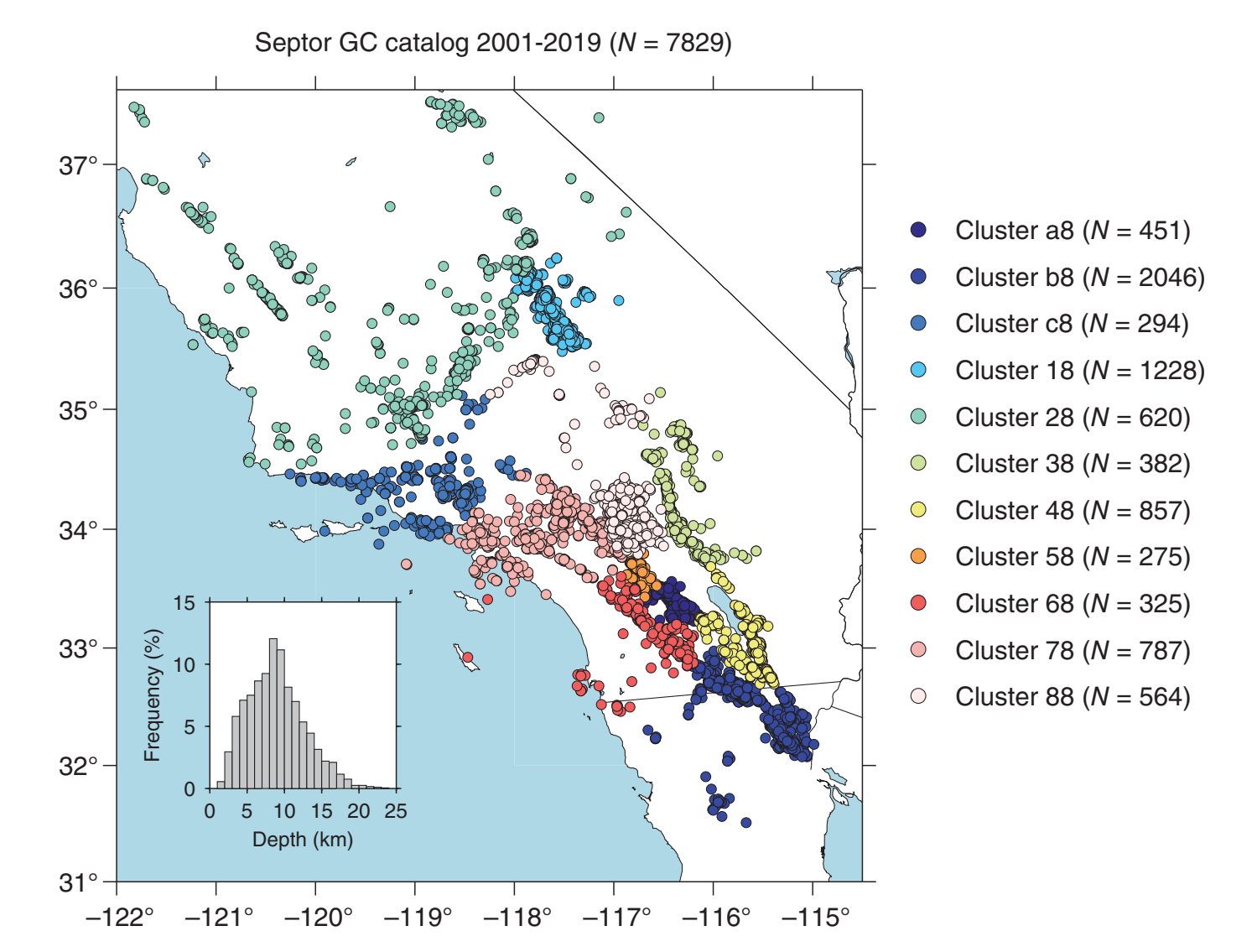
One approach to enhancing the robustness of deep learning models is to add physics-based parametric information to the training. The idea is that adding parametric information based on understandable physical concepts can prevent the over fitting of a deep learning model to data from a specific region. Kong et al. (2022) used a deep learning model to classify seismic sources either as earthquakes or explosions based on three-component seismograms and spectrograms. They found that for a given regional dataset, the deep learning model generally outperformed physics-based parametric discriminants such as Pg/Sg amplitude ratios. However, when a model trained with data from outside a region of interest was applied to that region, its performance suffered. The performance was comparable to or lower than that of *Pg/Sg* discrimination. The best overall performance was found when Pg/Sg ratios were explicitly combined with raw seismic data in the training of a two-branch deep learning model. In that case, the hybrid model outperformed the two individual discriminants in terms of transportability to new regions. A more general discussion of how human input can enhance the application of machine learning techniques in network seismology is given by Renouard et al. (2021).

In this study, we aim to determine whether depth sensitive parametric information exists for the small, locally recorded, earthquakes that were used to train Septor. If so, then that information might be used to make Septor more transportable to new regions. Such features might also be useful for direct depth estimation in areas that lack large training sets and dense seismic networks. For the Septor training catalog of 8359 well-located, southern California earthquakes, we examine four types of waveform features that are plausibly sensitive to focal depth. The first feature type is differential magnitudes. The difference between local magnitude (M_I) and coda duration magnitude (M_c) has been observed to have a weak dependence on the focal depth of tectonic earthquakes, with shallow earthquakes having enhanced generation of coda waves and thus relatively higher M_c (Holt et al., 2019). These observations are consistent with those of Mayeda and Walter (1996), who found extra peaking, or bumps, in coda wave spectra of especially shallow earthquakes and explosions, as discussed in Murphy et al. (2009). In this study, we additionally consider $M_{\rm w}$ - $M_{\rm c}$ differences. We calculate $M_{\rm L}$ and M_c using the automated methods described in Koper et al. (2021) and calculate M_0 (and thus M_w) using the Pg and Sg spectral modeling workflow described in Holt et al. (2021), which is based on the approach of Edwards et al. (2010). We presume that especially shallow earthquakes have smaller or more negative $(M_{\rm w}, M_{\rm L})$ - $M_{\rm c}$ values because of enhanced coda generation.

The Edwards et al. (2010) methodology assumes spectra can be fit by an ω^{-2} source model (Brune, 1970) with three free parameters: long-period spectral offset (Ω_0 , which can be converted into M_0), corner frequency (f_c) , and path averaged attenuation (t^*) . Although there is a well-known trade-off between f_c and t^* (e.g., Ko et al., 2012; Parolai and Oth, 2022), combinations of station averaged M_0 and f_c have been shown to be an effective measure of the relative frequency content in source spectra (e.g., Ataeva et al., 2017; Korrat et al., 2022). Previously, it has been observed that very shallow earthquakes are depleted in high-frequency energy relative to deeper crustal earthquakes because of lower near-source shear velocity (e.g., Allmann and Shearer, 2007). Even after accounting for this effect, there is evidence for depletion of high-frequency energy from shallow earthquakes (e.g., Hardebeck and Aron, 2009; Goebel et al., 2015; Trugman, 2020), although it is debated whether this is a true source effect (i.e., lower stress drop) or an artifact of the low-Q paths between shallow seismic sources and seismometers at local distances (e.g., Abercrombie et al., 2021; Shearer et al., 2022). Here, we use combinations of M_0 and f_c as a proxy for relative frequency content to test whether small, shallow earthquakes in southern California are uniformly depleted in high-frequency energy.

A useful byproduct of the Holt *et al.* (2021) $M_{\rm w}$ workflow is the Pg and Sg spectral amplitudes. P/S amplitude ratios are most well known for being an effective discriminant of explosions and earthquakes (e.g., Bowers and Selby, 2009); however, there is some evidence that P/S amplitude ratios are sensitive to source depth (Taylor *et al.*, 1989; Goldstein, 1995; Myers *et al.*, 1999). We evaluate that possibility in this study using Pg/Sg spectral amplitude ratios in three narrow frequency bands of 3–5, 5–6.5, and 6.5–8 Hz. The fourth waveform feature we consider is Rg/Sg amplitude ratios, which several authors have found to be useful as a depth discriminant (e.g., Kafka, 1990; Kolaj, 2018; Tibi *et al.*, 2018, Kinter *et al.*, 2020).

In the following sections, we first provide details on the dataset of southern California earthquakes used in Septor. We then describe calculations of M_L and M_c for the dataset, including a comparison to catalog magnitudes provided by the Southern California Earthquake Data Center (SCEDC). We examine the sensitivity of M_L - M_c to focal depths for various subsets of the Septor dataset, similar to the regionalization approach used in Italy by Holt et al. (2019). Next, we describe calculations of M_0 and f_c for the dataset, including comparisons to $M_{\rm w}$ values provided by SCEDC for the ~100 largest earthquakes and $M_{\rm w}/M_{\rm L}$ comparisons for the whole dataset. Similar to the M_L – M_c analysis, we examine M_w – M_c for depth sensitivity. We also examine how a proxy for relative frequency content, $\Phi \equiv \log_{10}(M_0) + 3\log_{10}(f_c)$, varies with source depth. Following that, we describe calculations of amplitude ratios (Pg/Sg and Rg/Sg) and their correlation with source depth. We conclude with multilinear regression analysis to quantify how well the physics-based features perform at explaining



earthquake depths in Southern California and the advantage provided by combining features.

THE SEPTOR DATASET OF SOUTHERN CALIFORNIA EARTHQUAKES

The Septor dataset comprises 8359 earthquakes that occurred in southern California during 1 January 2001-31 December 2019 (Siddiquee et al., 2022). The earthquakes are small-to-moderate sized (2 $< M_{\rm L} <$ 4) and were chosen partially based on proximity to a nearby station, which improves depth resolution. The hypocenters were derived using a complex process that involves analyst picks, source-specific station terms, waveform derived differential arrival times, cluster analysis, and relative relocation (Lin et al., 2007; Hauksson et al., 2012). Over 93% (7829) of the earthquakes were members of one of 11 geographical clusters "gc," which were created during relative relocation with Growclust (Trugman and Shearer, 2017; Fig. 2). Cluster size ranged from 275 to 2046. The two largest clusters correspond to the 2019 Ridgecrest sequence (e.g., Ross et al., 2019) and the 2010 El Mayor-Cucapah sequence (e.g., Wei et al., 2011). About 7% (530) of the earthquakes were individually located within a

Figure 2. Epicenters of the 7829 earthquakes in the *Septor* dataset that have been relatively relocated into 11 clusters. The inset shows the combined distribution of focal depths.

3D velocity model. These events have slightly less well-resolved depths—42% have a ratio of nearest station distance (dmin) to focal depth (h) over 1.5—and are removed from further analysis. We were able to identify preferred magnitude types for all the "gc" earthquakes. The vast majority were $M_{\rm L}$ (7546) followed by $M_{\rm w}$ (112).

We acknowledge that some inaccuracies in depth may still be present in the *Septor* dataset, perhaps because of the effect of magnitude differences in relative relocation (e.g., Bachura and Fischer, 2019), inaccurate Earth models (e.g., Diehl *et al.*, 2021), and evolving or variable network geometries (e.g., Lee *et al.*, 2023). However, given the station density in southern California, the sophistication of the location procedures described earlier, and the selection criteria applied in Siddiquee *et al.* (2022), we assume that most of the *Septor* depths are well resolved enough to be used as training data in this study.

COMPUTATION OF PHYSICS-BASED WAVEFORM FEATURES

Local magnitudes and coda duration magnitudes

We calculated local magnitude (M_L) and coda duration magnitude (M_c) using the automated methodology described in Koper et al. (2021). For each earthquake, waveforms were downloaded from the Incorporated Research Institutions for Seismology Data Management Center (IRIS-DMC) for high gain channels located 10-150 km from the epicenter. Event magnitudes were calculated from the median of station values when data from at least three stations were successfully processed. There were 7425 successful $M_{\rm L}$ calculations, 7509 successful M_c calculations, and 7392 earthquakes for which both magnitudes were calculated (Fig. S1, available in the supplemental material to this article). The median number of stations used in the magnitude calculations was 20 for $M_{\rm L}$ and 28 for $M_{\rm c}$. The automated $M_{\rm L}$ values are highly correlated with the corresponding values from the SCEDC earthquake catalog and have a bias of just 0.01 magnitude units. There are no catalog M_c values to compare with the automated M_c values, but the automated M_c values are highly correlated with M_L . M_c appears to be slightly saturated, probably because of the high attenuation in southern California and the fact that we use high frequencies (≥1 Hz) to generate the coda envelopes on which duration is based. M_c values are systematically smaller than M_L values by 0.37 magnitude units, reflecting the fact that our procedure for calculating M_c was designed to produce an unbiased proxy for $M_{\rm L}$ in Utah, where wave propagation is different.

We present the variation of $M_{\rm L}$ – $M_{\rm c}$ with source depth for each of the 11 relatively relocated "gc" clusters in Figure 3. The correlation coefficient is positive at significance levels above 99% for 8 of the 11 "gc" clusters and above 95% for a ninth cluster. The corresponding slopes are in the range of 0.01–0.05 magnitude units per kilometer, consistent with the results of Holt et al. (2019) for earthquakes in Utah, Yellowstone, Oklahoma, and Italy. Cluster "b8", which includes the 2010 El-Mayor Cucapah sequence in Baja, Mexico, is the only 'gc' cluster with a statistically significant negative correlation. There appears to be a break in the depths within 'b8' around 10 km, with the deeper events having noticeably smaller M_L – M_C values.

To check for robustness, we repeated our analysis for all the geographic clusters using a maximum depth of 10 km, instead of 20 km, and found qualitatively similar results. We also divided the dataset into subsets according to distance and found similar results using ranges of 10–50 km (Fig. S2) and 10–100 km (Fig. S3). For the 10–50 km distance range, the deeper events in the problematic "b8" cluster were removed and the correlation turned slightly positive, although not above the 95% threshold. As a final test we recalculated coda durations at all the stations using a slightly lower passband, 0.5–10 Hz instead of 1.0–10 Hz (Fig. S4). We found that $M_{\rm c}$ saturation was mitigated in the lower passband, consistent with the observation that coda durations increase at longer periods (Mayeda and Walter, 1996).

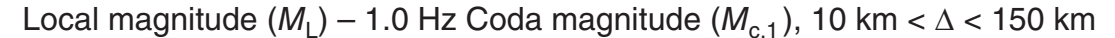
Interestingly, we also found that the positive correlation between $M_{\rm L}$ – M_c and depth increased in most regions with a median change of +33.5% in correlation coefficients. In cluster "18," which includes the 2019 Ridgecrest sequence, the correlation coefficient doubled from 0.09 to 0.18. We conclude that in southern California shallow earthquakes tend to have enhanced M_c values, leading to smaller $M_{\rm L}$ – M_c values. As depth increases, M_c is less enhanced, and $M_{\rm L}$ – M_c values gradually become more positive, consistent with $M_{\rm L}$ – M_c observations made in other regions (Holt *et al.*, 2019).

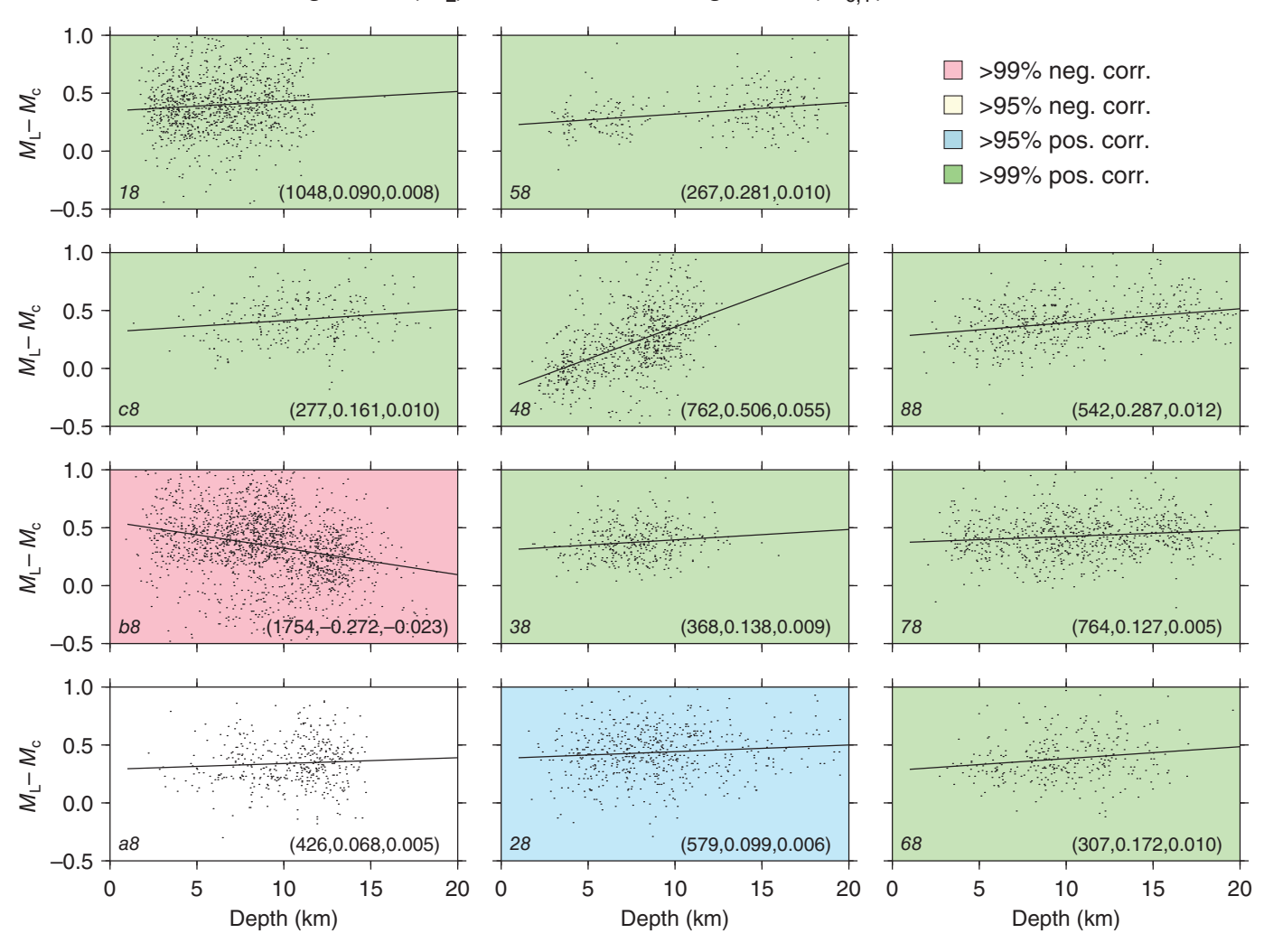
The modest sensitivity of M_L-M_c to focal depths of southern California earthquakes is evident without using station corrections, regionally specific distance corrections, or analyst reviewed amplitude and duration measurements. Thus, the depth sensitivity shown here should be considered a lower bound; correction of site and path effects would probably lead to significantly stronger depth sensitivity in southern California. It is also likely that more complex functions of M_c and M_L would show greater depth sensitivity (Holt, 2021), and we return to this point later in the Bilinear regression of modified waveform features section.

Source models from Pg and Sg spectra

Observation and modeling of body-wave spectra are commonly used to infer source properties of small-magnitude seismic events recorded at local and regional distances. Spectra reflect source, path, and site effects, with various methods used to isolate the signature of the source (e.g., Kemna et al., 2021). Empirical Green's functions are used to eliminate path and site effects when smaller events with simple source properties are collocated with larger, more complicated events (e.g., Mueller, 1985; Hough, 1997). Formal generalized inversions are used across broad regions to partition source, path, and site effects (e.g., Shearer et al., 2006; Oth et al., 2017; Shible et al., 2022). Here, we choose the simple approach of modeling individual spectra, because we are primarily interested in empirical properties of spectral shapes rather than interpreting physical source properties such as stress drop. Our hypothesis is that spectra from especially shallow earthquakes will be observably depleted in high frequencies because of low velocity and high attenuation at shallow depths (e.g., Brocher, 2008). However, our approach also provides stable $M_{\rm w}$ estimates, which we use in place of M_L to verify the enhancement of M_c for shallow earthquakes reported in the previous section.

We use a spectral fitting method designed for estimating $M_{\rm w}$ of small earthquakes recorded by the Swiss regional seismic network (Edwards *et al.*, 2010). Our implementation is a simplified version of the automated workflow described in Holt *et al.* (2021). We used broadband data for stations within 150 km of earthquakes in the *Septor* database. Pg and Sg arrival times were defined using group velocities of 6.0 and 3.4 km/s, respectively. The Pg window starts before the Pg arrival and ends at 0.75 of the Sg–Pg time difference. The Sg window starts





at 0.90 of the Sg-Pg time difference and has a duration of 20 s. Both Pg and Sg windows are further modified using the integral of the squared amplitudes in the window and refining the start and end times based on the first and the 99th integral percentile. Spectra were calculated using a multitaper approach over a variable width frequency band that was defined by amplitude relative to the noise immediately preceding Pg. Individual velocity spectra were fit using a Brune source model with three free parameters: long-period spectral offset (Ω_0) , apparent corner frequency (f_c) , and path-averaged attenuation (t^*) . To mitigate the trade-off between f_c and t^* , a second stage of spectral fitting involved fixing f_c and allowing Ω_0 and t^* to freely vary. Ω_0 was converted into \boldsymbol{M}_0 using near-source elastic values from a 1D Earth model (Western U.S. [WUS], Herrmann et al., 2011) and assuming 1/R geometrical spreading, in which R is source–receiver distance. M_0 was converted to M_w using the standard relationship (Hanks and Kanamori, 1979). The event f_c in the first stage of the spectral fitting was determined using a weighted average of the station f_c values, for which weights were inversely related to R. No site or path corrections were used.

Figure 3. Variation in $M_L - M_c$ versus focal depth for earthquakes in the 11 *Septor* subgroups. The italicized text in the lower left indicates the specific cluster as shown in Figure 2. The triple of numbers in the lower right indicates the number of events, the correlation coefficient, and the slope of a best-fitting line, respectively. Color indicates the probability of the correlation being significantly positive (green, blue) or negative (red, yellow), according to a standard Student's t-test. The confidence levels are conservative because we assume N = 100 to compute the t-value.

We were successful in estimating $M_{\rm w,S}$ and $f_{c,S}$ for 7389 earthquakes and $M_{\rm w,P}$ and $f_{c,P}$ for 6476 earthquakes (Fig. 4). An example spectral fit is presented in Figure S5. The modeling was considered successful if there were at least three stations, and the standard error of the $M_{\rm w}$ estimate was less than 0.25. The two $M_{\rm w}$ estimates are highly similar with a correlation coefficient of 0.97 and a bias of only 0.02 m.u. The two f_c estimates have more scatter (correlation coefficient of 0.37), as might be expected from trade-offs with $t^{\star}f_{c,P}$ has higher variance than $f_{c,S}$, leading to a long tail in the distribution of $f_{c,P}/f_{c,S}$ ratios. Nevertheless, the modal value of 1.4 for $f_{c,P}/f_{c,S}$ is similar to the median value of 1.5 for 717 tectonic earthquakes in the

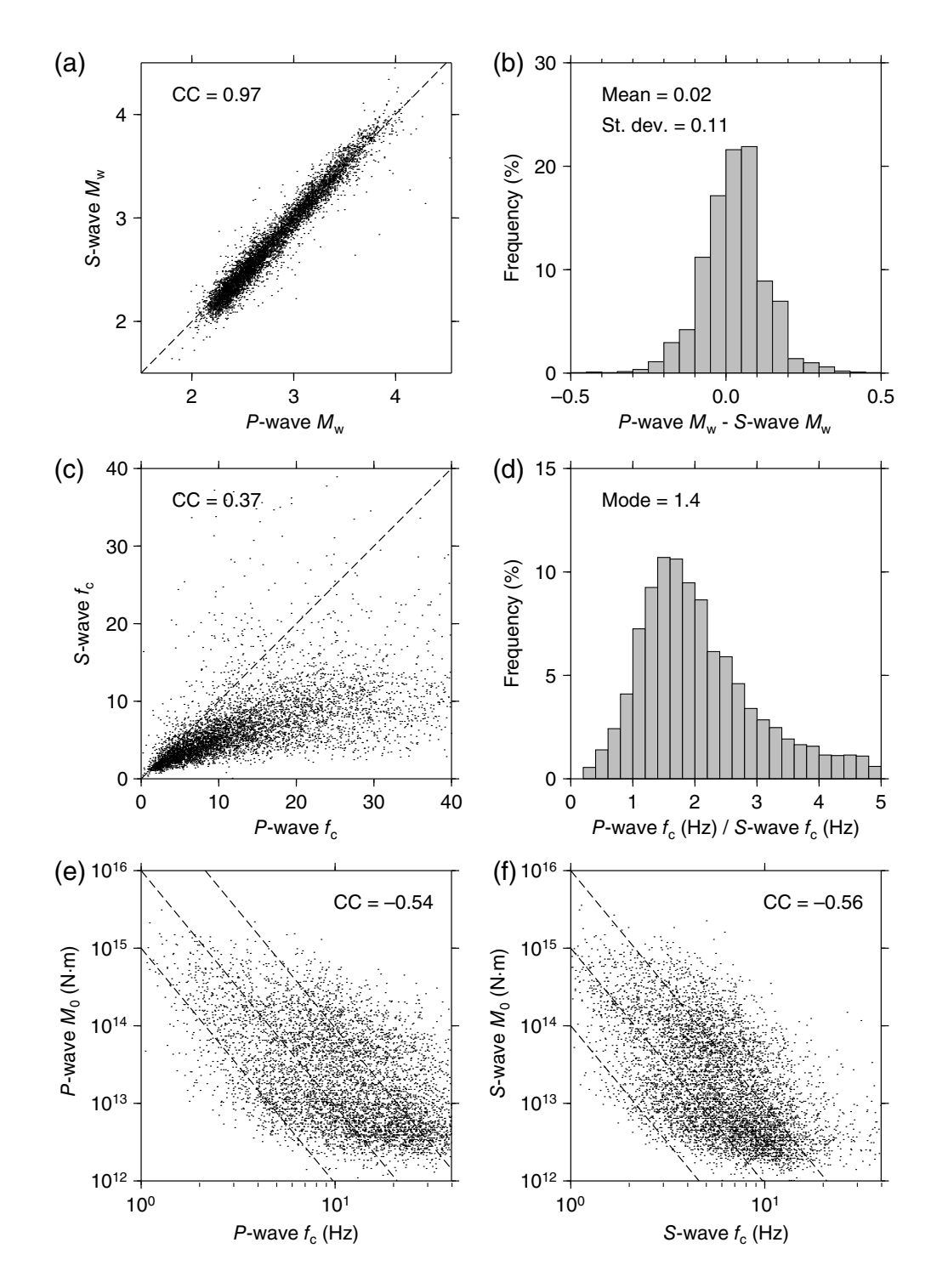


Figure 4. Summary of automated Pg and Sg spectral fits for the Septor dataset of southern California earthquakes. (a) Comparison of S-wave M_w with P-wave M_w . A 1:1 dashed line is shown for reference. (b) Distribution of residuals between the two M_w estimates. (c) Comparison of S-wave f_c with P-wave f_c . A 1:1 dashed line is shown for reference. (d) Distribution of P-wave f_c /S-wave f_c ratios. (e) Comparison of M_0 and M_0 for M_0 waves. The dashed lines indicate a constant apparent stress drop. The spacing between the lines represents a factor of 10 change in apparent stress drop. (f) Comparison of M_0 and M_0 are M_0 waves. The dashed lines are like those in panel (e).

southern Apennines of Italy (Zollo *et al.*, 2014), 1.4 for 90 induced earthquakes in Texas (Jeong *et al.*, 2020), 1.2 for 226 earthquakes in Israel (Ataeva *et al.*, 2017), 1.2–1.3 for 440 earthquakes in Egypt (Korrat *et al.*, 2022), and 1.3 for ~100

earthquakes southern California (Abercrombie, 1995). As expected, $\log_{10}(M_0)$ is negatively correlated with $\log_{10}(f_c)$ for both P and S data, with scatter approximately bounded by two orders of magnitude change in apparent stress drop. This level of $\log_{10}(M_0)$ versus $\log_{10}(f_c)$ scatter is only slightly greater than in studies conducted with more sophisticated methods (e.g., Kemna et al., 2021).

The spectral $M_{\rm w}$ values we calculate are remarkably consistent with SCEDC $M_{\rm w}$ values, which are determined via moment tensor waveform inversion, considering we are using a simple geometrical spreading model and no site corrections. For the 111 earthquakes in the Septor database with an SCEDC catalog $M_{\rm w}$, we find a correlation coefficient of 0.86 between $M_{\rm w,SCEDC}$ and $M_{w,P}$ and a bias under 0.01 m.u. (Fig. S6). Our spectral Mw.P values also closely track $M_{\rm L,SCEDC}$, with a correlation coefficient of 0.93. The slope is close to 1:1 for magnitudes above $M_{\rm L} \sim 3.0$ and noticeably flattens at smaller magnitudes consistent with theoretical expectations (e.g., Deichmann, 2017). The results in Figure 4 and Figure S6 give us confidence that our spectral modeling results are robust, even though we did not inspect and customize individual Pg and Sg time windows.

Sensitivity of M_w – M_c to focal depth. The correlation coefficient between $M_{w,P}$ – M_c and source depth is positive

in 9 of 11 geographical regions (Fig. S7), as expected for $M_{\rm c}$ enhancement in shallow earthquakes. In four of the regions the positive correlation is significant at the 99% level, and in a fifth region it is significant at the 95% level. As with

the $M_{\rm L}$ – $M_{\rm c}$ results shown in Figure 3, cluster b8 in the Baja region is anomalous with a strong negative correlation, and cluster 48 near the Salton Sea is the most positively correlated. If we use the lower frequency version of $M_{\rm c}$, the correlations between $M_{\rm w,P}$ and $M_{\rm c}$ and source depth become noticeably stronger (Fig. S8), similar to our $M_{\rm L}$ – $M_{\rm c}$ observations. Analogous, but weaker, correlations are obtained between $M_{\rm w,S}$ – $M_{\rm c}$ and depth (Figs. S9, S10). In general, these results reinforce the idea that it is mainly abnormally large $M_{\rm c}$ values, as opposed to abnormally small $M_{\rm L}$ values, that create smaller, or more negative, $M_{\rm L}$ – $M_{\rm c}$ values for shallow earthquakes.

Sensitivity of relative frequency indicators to focal depth. The relative amount of high-frequency energy radiated by an earthquake is related to the stress drop $(\Delta \sigma)$ of the source. All things being equal, high stress drop earthquakes radiate more high-frequency energy. A commonly used earthquake source model (Eshelby, 1957) states that

$$\Delta \sigma = K M_0 (f c/\beta)^3, \tag{1}$$

in which K is a geometrical constant, and β is the shear velocity in the source region. Taking the logarithm of both sides and rearranging terms gives

$$\log_{10}(M_0) + 3\log_{10}(f_c) = \log_{10}(\Delta\sigma) + 3\log_{10}(\beta) - \log_{10}(K).$$
(2)

Because $\Delta \sigma$ and especially β are expected to increase with depth, and K is expected to be independent of depth, we expect that the observable quantity on the left side will be positively correlated with source depth. We define this quantity as

$$\Phi \equiv \log_{10}(M_0) + 3\log_{10}(f_c), \tag{3}$$

and use it to gauge the relative frequency content in a spectrum, with higher values indicating enrichment in high-frequency energy. We measure it separately for P waves (Φ_P) and S waves (Φ_S) . Figure 5 shows the relationship between Φ_P and focal depth for the 11 Septor geographical regions. The correlation coefficient is positive for 9 of 11 regions and is significant above the 99% level for 7 of the 9. Similar, although somewhat weaker, results are found for Φ_S (Fig. S11).

Our relative frequency indicator Φ seems roughly as sensitive to focal depth as $M_{\rm L}$ – $M_{\rm c}$ or $M_{\rm w}$ – $M_{\rm c}$. However, a concern is that when converting the long-period spectral offset Ω_0 to scalar moment M_0 we assume knowledge of the source depth to calculate the near-source velocities in the WUS model. Therefore, the correlations shown in Figure 5 and Figure S11 might be overly optimistic compared to what would be achieved in a setting when the source depth and near-source velocity model are poorly known. To address this issue, we repeated all the spectral

fitting using a half-space model, instead of WUS, to convert Ω_0 into M_0 . For the half-space, we choose values from the third layer of WUS ($P=6.27~{\rm km/s},~S=3.74~{\rm km/s},~\rho=2780~{\rm kg/m^3}$), which corresponds to the depth range of 8–21 km. Using the updated values of M_0 , we find results almost identical to those from before, but with slightly stronger correlations. Therefore, detailed prior knowledge of the velocity structure near the source is not needed to use Φ as a depth predictor.

Sensitivity of Pg/Sg amplitude ratios to focal depth.

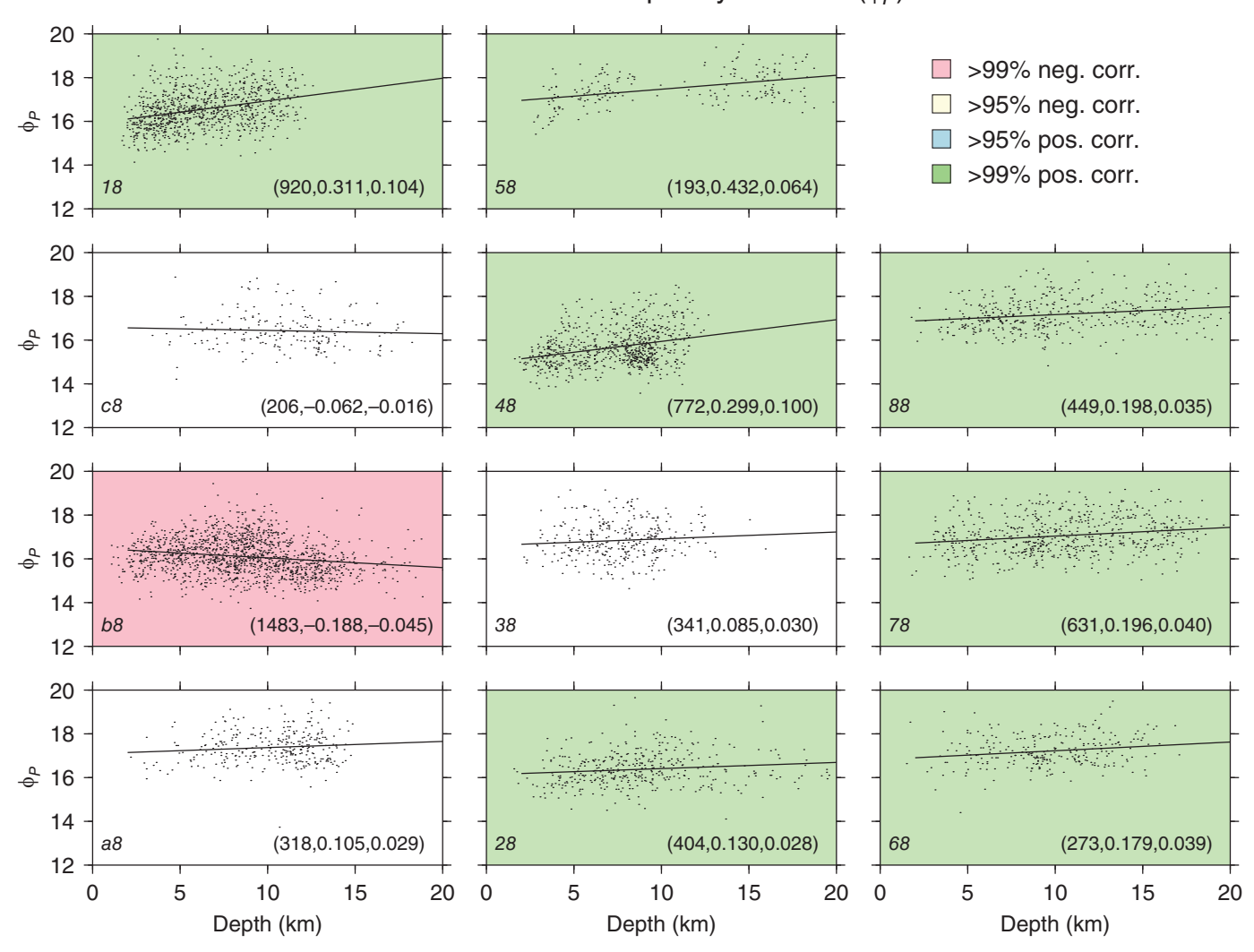
High-frequency P/S amplitude ratios are well known to be an effective source discriminant at regional distances, especially when ratios from many stations can be averaged together for individual sources (e.g., Bowers and Selby, 2009). The method can be improved by correcting individual P and S amplitudes for differences in magnitudes and path and propagation effects, which is often referred to as "MDAC," for Magnitude and Distance Amplitude Corrections (e.g., Taylor et al., 2002; Walter and Taylor, 2002). Variations in event depth are recognized as a factor that might affect P/S amplitude ratios; however, depth is usually not explicitly corrected for. Instead, it is treated as an added source of uncertainty (e.g., Anderson et al., 2009). Source depth could systematically affect *P/S* amplitude ratios in various ways: if high-frequency S(Lg) energy is preferentially attenuated at shallow depths (e.g., Baker et al., 2004), if P/S velocity ratios change significantly with depth, or if isotropic radiation from material damage (Ben-Zion and Ampuero, 2009) varies with depth.

We calculated Pg/Sg amplitude ratios by averaging amplitude spectra of ground velocity in three distinct frequency bands: 3-5, 5-6.5, and 6.5-8 Hz. P and S energy in each band was required to satisfy the signal-to-noise ratio (SNR) requirement for spectral fitting before the ratio was calculated, and these bands yielded the most observations. P spectra were calculated from the vertical component and S spectra from the transverse component. Event averages were accepted when valid measurements were available from three or more stations. No corrections for distance, magnitude, or site effects were applied. Figure 6 shows the relationship between the lowest frequency Pg/Sg amplitude ratios and focal depth in each of the 11 regions. Seven regions have a negative correlation coefficient that is significant above the 99% level, three regions have no significant correlation, and only region 38 has a significantly positive correlation coefficient. Similar results are observed for the middle (Fig. S12) and higher frequency (Fig. S13) bands.

Rg/Sg amplitude ratios

Short-period Rayleigh waves (*Rg*) are usually well-observed only for events shallower than 3–4 km (e.g., Kafka, 1990), hence detection of *Rg* can be used as a depth discriminant (e.g., O'Rourke and Baker, 2017). To the best of our knowledge, Tibi *et al.* (2018) is the only study that demonstrates a steady

P-wave relative frequency indicator (ϕ_P)



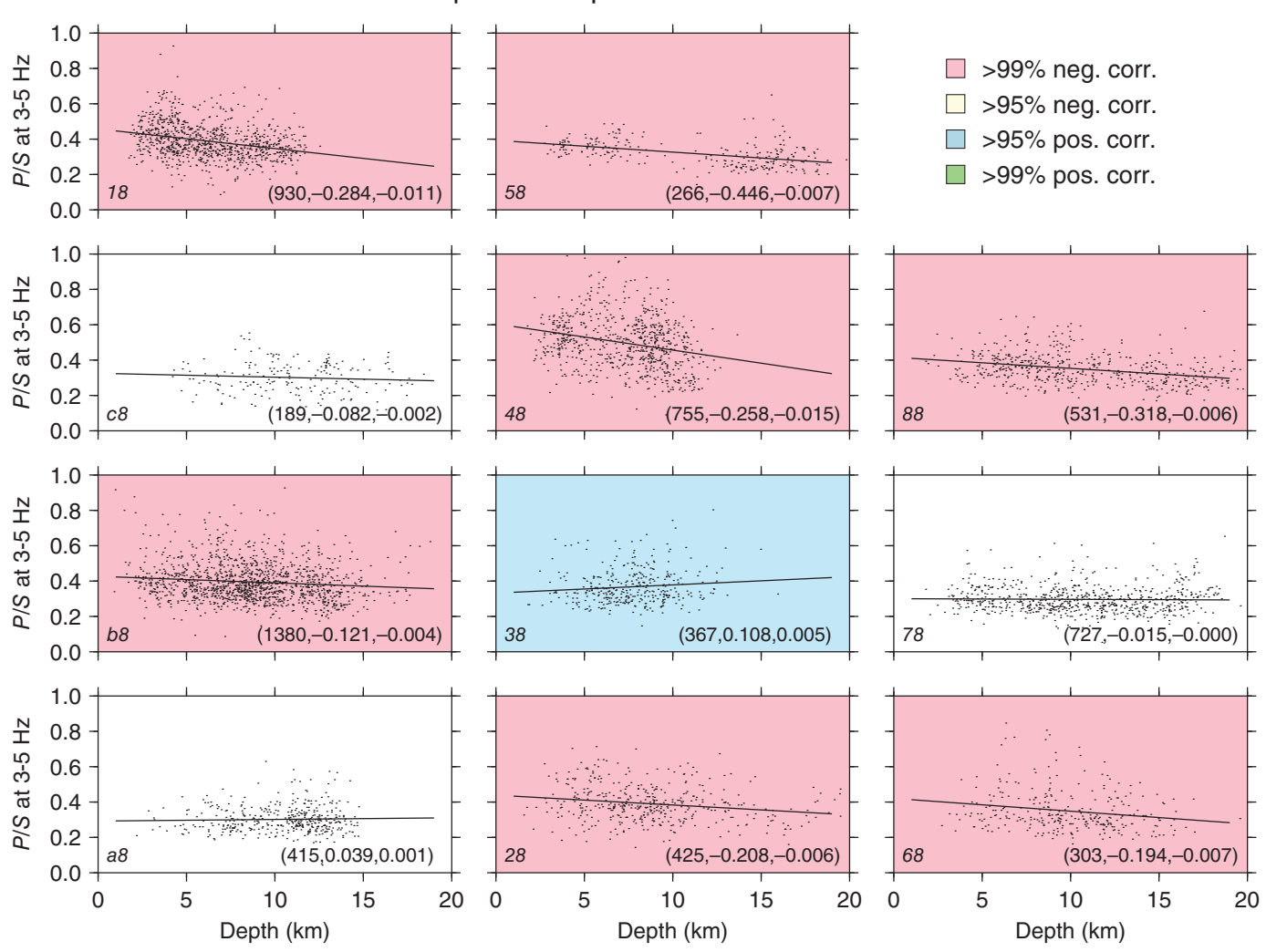
decrease in Rg/Sg amplitude ratio as earthquake depth increases. They not only find much higher Rg/Sg amplitude ratios for extremely shallow (<1 km) earthquakes, in which Rg is easily visible, but also a steady trend of decreasing Rg/Sg amplitude ratios as focal depth increases from 2 to 12 km, in which Rg is not as well observed. For the deeper events, we speculate that the Rg time window is composed mostly of Sg coda energy, and that Rg/Sg devolves into Sg,coda/Sg,direct, which is expected to decrease with depth analogous to how M_L-M_c increases with depth. Furthermore, the "Rg" energy is measured at 0.5–2 Hz, whereas the Sg,direct energy is measured at 0.5–8 Hz, so the amplitude ratios should tend to decrease with depth because of the relative depletion in high-frequency energy for shallow earthquakes, as observed with Φ .

We used a modified version of the procedure described in Tibi *et al.* (2018) to calculate $\log_{10}(Rg/Sg)$ for 5129 earth-quakes in the *Septor* dataset using an Rg group velocity of 2.0 km/s. Individual amplitudes are measured from smoothed time series derived from spectrograms, and the amplitude ratio is computed if the SNR is greater than 2 for both phase amplitudes, with noise defined from a pre-P time window. An

Figure 5. Variation in the *P*-wave relative frequency indicator, $\Phi_P = \log_{10}(M_{0,P}) + 3\log_{10}(f_{c,P})$, versus focal depth for earthquakes in the 11 *Septor "gc"* clusters. M_0 has units of N·m, and f_c has units of hertz. The italicized text in the lower left indicates the specific cluster as shown in Figure 2. The triple of numbers in the lower right corresponds to the number of events, the correlation coefficient, and the slope of a best-fitting line, respectively. Color indicates the probability of the correlation being significantly positive (green, blue) or negative (red, yellow) according to a standard Student's *t*-test. The confidence levels are conservative because we assume N = 100 to compute the *t*-value.

example measurement is presented in Figure S14. Amplitude ratios for individual events are computed when valid ratios from three or more stations are available to average. In general, Rg is rarely observed clearly, even for earthquakes with depths < 3 km, consistent with the high-crustal attenuation in southern California and the tendency for Rg to quickly attenuate with distance (e.g., Myers *et al.*, 1999). We experimented with Rg group velocities between 1.5 and 2.5 km/s but did not find significant changes to Rg/Sg amplitude ratios. We did not attempt to correct the amplitude ratios for differences in

P/S spectral amplitude ratio at 3.0 – 5.0 Hz



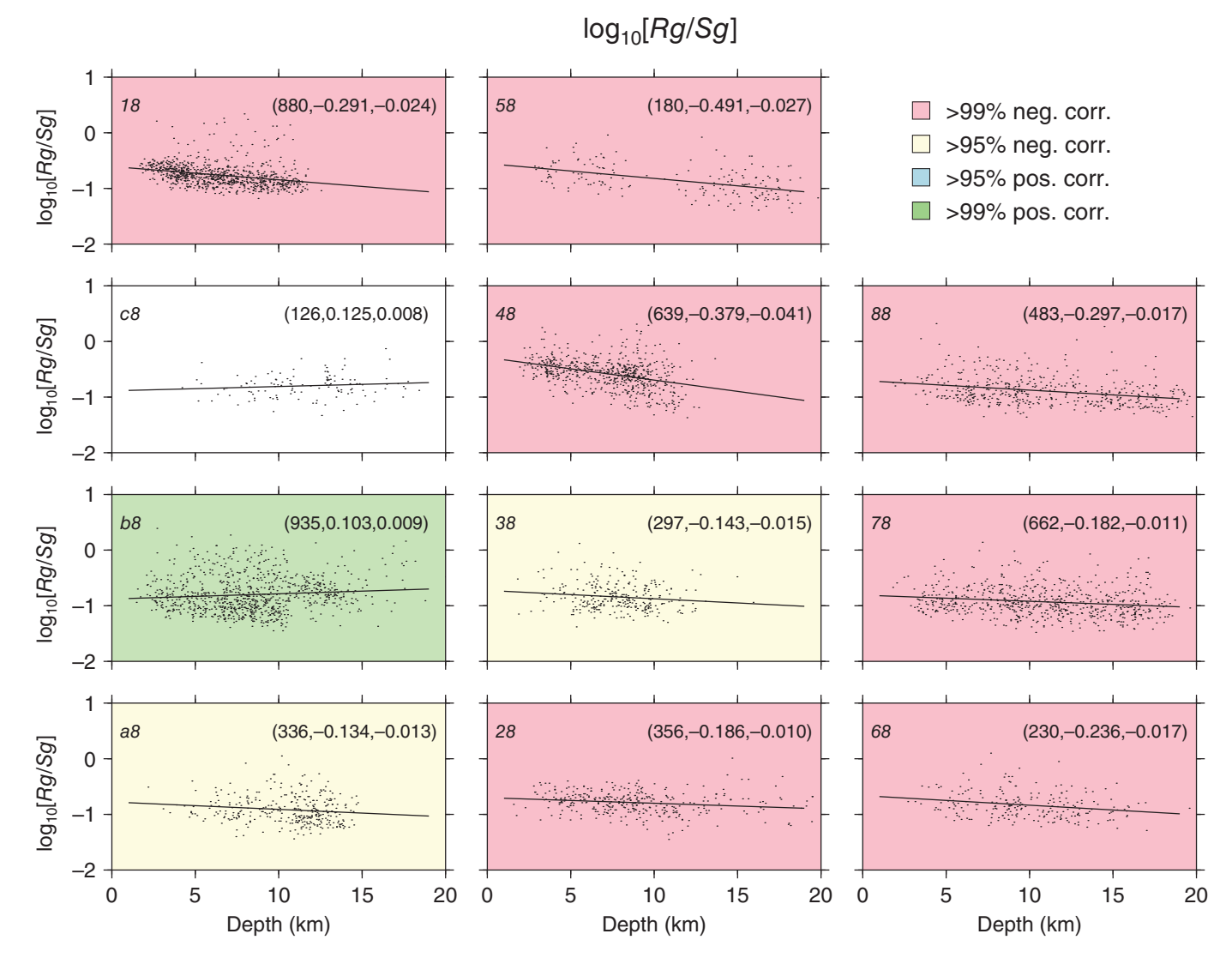
geometrical spreading or attenuation (e.g., Kinter *et al.*, 2020; Tibi *et al.*, 2023) because of the likelihood that we are mainly observing Sg coda waves in the Rg time window. The dependence of $\log_{10}(Rg/Sg)$ on depth for each geographical region is presented in Figure 7. Nine of the 11 regions have significantly negative correlations, one region is uncorrelated, and the problematic region (b8) shows opposite (positively correlated) behavior.

DEVELOPMENT OF FEATURE-BASED MODELS FOR PREDICTING FOCAL DEPTH

For three of the four types of physics-based waveform features $(M_{\rm L}/M_{\rm w}-M_{\rm c}, \Phi, Pg/Sg,$ and Rg/Sg), the depths in region b8 stand out as anomalous. For differential magnitudes, depths in b8 are negatively correlated, whereas in all other regions the correlation is positive or not significant (Fig. 3, Figs. S2–S4, S7–S10). The same behavior is seen for Φ_P and Φ_S (Fig. 5, Fig. S11). For Rg/Sg amplitude ratios the relationship is inverted; depth is positively correlated with amplitude ratios in b8 but is negatively correlated or uncorrelated in nearly every other region (Fig. 7). Figure 8 shows event locations in region b8,

Figure 6. Variation in Pg/Sg spectral amplitude ratio at 3–5 Hz versus focal depth for earthquakes in the 11 *Septor "gc"* clusters. The italicized text in the lower left indicates the specific cluster as shown in Figure 2. The triple of numbers in the lower right corresponds to the number of events, the correlation coefficient, and the slope of a best-fitting line, respectively. Color indicates the probability of the correlation being significantly positive (green, blue) or negative (red, yellow) according to a standard Student's *t*-test. The confidence levels are conservative because we assume N = 100 to compute the *t*-value.

which mainly consists of aftershocks of the 2010 $M_{\rm w}$ 7.2 El Mayor–Cucapah earthquake. The sequence can be divided into two main clusters with the southeastern cluster noticeably deeper. However, as discussed in Hauksson *et al.* (2011), station density decreases dramatically south of the United States–Mexico border with corresponding increases in location uncertainty toward the southeast. We speculate that instead of being deeper, the southeastern aftershocks are shallower than the better located aftershocks to the northwest. Shallowing of depths to the southeast might be expected as one nears oceanic crust in the Gulf of California. Furthermore, if the southeastern cluster of



events in b8 is removed, by implementing a source–receiver distance cutoff of 50 km for magnitude calculation, the anomaly in $M_{\rm L}$ – $M_{\rm c}$ versus depth disappears (Fig. S2). Hence, we feel justified in eliminating earthquakes in region b8 from further analysis.

Linear regression of individual waveform features

We use linear regression to compare the sensitivities of our physics-based features to focal depth. Here, focal depth is treated as the dependent variable, and the features are treated as the independent predictor variables. Some of the features are highly correlated, which can cause instability in multilinear regression. For instance, the high correlation between $M_{\rm w,P}$ and $M_{\rm w,S}$ (0.97) means that the features $M_{\rm w,P}-M_{\rm L}$ and $M_{\rm w,S}-M_{\rm L}$ are also highly correlated. Similarly, for features involving the higher (>1 Hz) and lower (>0.5 Hz) frequency coda duration magnitudes $M_{\rm c,1}$ and $M_{\rm c,2}$. Therefore, we start with a series of 132 linear models relating each feature (f_i) to depth in each data group (d_i) ,

$$d_i = m_{0ij} + m_{1ij} \times f_i, \tag{4}$$

Figure 7. Variation in $\log_{10}(Rg/Sg)$ amplitude ratio versus focal depth for earthquakes in the 11 *Septor "gc"* clusters. The italicized text in the upper left indicates the specific cluster as shown in Figure 2. The triple of numbers in the upper right corresponds to the number of events, the correlation coefficient, and the slope of a best-fitting line, respectively. Color indicates the probability of the correlation being significantly positive (green, blue) or negative (red, yellow) according to a standard Student's *t*-test. The confidence levels are conservative because we assume N = 100 to compute the *t*-value.

in which i is one of the 12 waveform features described previously, j is one of the 11 data groups, m_{0ij} is the intercept, and m_{1ij} is the slope. We use 10 of the 11 geographical clusters (Fig. 2) as data groups (omitting cluster b8) and generate the 11th, regionally balanced, data group (designated as DS) by randomly selecting 100 events from each of the 10 acceptable geographical clusters. The quality of each feature f_i can be measured by the coefficient of determination (R^2), which is the fraction of variance in depths d_j it can explain. The significance of each feature can be assessed by its p-value using an F test, which accounts for varying degrees of freedom. Low p-values

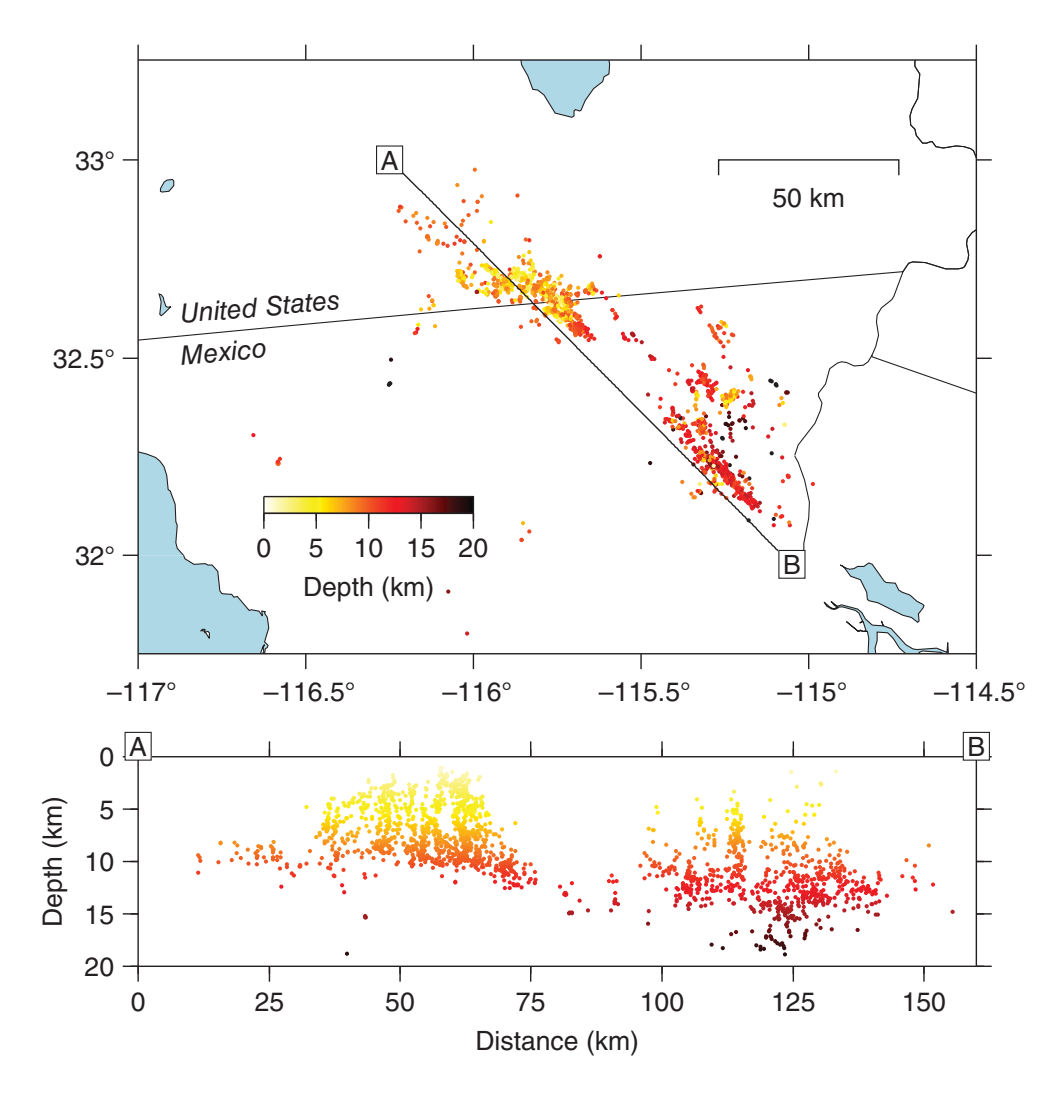


Figure 8. Distribution of earthquakes in the region "b8" of the *Septor* dataset (Fig. 2). Most of these events are aftershocks of the 2010 **M** 7.2 El Mayor—Cucapah sequence. We interpret the deepening of focal depth toward the southeast as an artifact of decreased seismometer density south of the United States—Mexico border. These events are outside of the main Southern California Seismic Network footprint and so have lower location accuracy.

imply that the null hypothesis—no correlation between the feature and depth—can be rejected with high confidence.

The R^2 values from the 132 linear regressions involving individual features are reported in Figure 9 (rows 1–12). R^2 varies between 0.00 and 0.33 and 83 (63%) of the models have p-values less than 0.01, indicating the correlation is significant with a high degree of confidence. The p-values are reported in Figure S15, and they track R^2 values closely enough that differences in R^2 alone can be used to rank and compare the 12 two-parameter models (designated as M 2.1, 2.2, ..., 2.12). Models using $M_{c,2}$ generally perform better than models using $M_{c,1}$: model M 2.2 outperforms model M 2.1 in all 11 data groups, M 2.4 outperforms M 2.3 in 6 of 11 data groups, and model M 2.6 outperforms M 2.5 in 10 of 11 data groups. As discussed earlier, the lower frequency cutoff of 0.5 Hz used for $M_{c,2}$ better captures coda durations in the highly attenuating crust of southern California. Overall, the differential

magnitude models based on $M_{\rm L}$ - $M_{\rm c}$ (M 2.1 and 2.2) perform better than the models based on $M_{\rm w}$ - $M_{\rm c}$ (M 2.3, 2.4, 2.5, and 2.6). The region averaged R^2 values are (0.055, 0.084) for the former models and (0.039, 0.039, 0.031, and 0.039) for the latter. The Pwave relative frequency indicator, $(\Phi_P, \mathbf{M} 2.7)$ performs slightly better than its S-wave counterpart (Φ_S , M 2.8). M 2.7 has a region averaged R^2 of 0.051 and p < 0.01 in 8 of 11 data groups, whereas M 2.8 has a region averaged R^2 of 0.048 and p < 0.01 in 6 of 11 data groups. The models based on Pg/Sg amplitude ratios do better at lower frequencies. The best is M 2.10 at 3-5 Hz with averaged R^2 of 0.057 and p < 0.01 in 7 of 11 regions, next is M 2.11 at 5-6.5 Hz with averaged R^2 of 0.038 and p <0.01 in 6 of 11 regions, and last is M 2.12 at 6.5-8 Hz with averaged R^2 of 0.023 and p <0.01 in 5 of 11 regions. Overall, M 2.2 has the highest region averaged R^2 at 0.083, followed by M 2.9 at 0.074, and M 2.10 at 0.057, but no individual model performs best across all regions. For example,

model M 2.3 is best in region a8, model M 2.2 is best in region c8, model M 2.8 is best in region 18, model M 2.9 is best in region 58, and model M 2.6 is best in region 88.

Figure 9 also shows how depth predictability varies with geographical region. For instance, in region c8 only 2 of 12 models yield p < 0.01, and the model averaged R^2 value is 0.008. Region c8 is composed of events near the Santa Barbara channel, which are located with relatively large azimuthal gaps and might have less well resolved depths. Region 38 also has low depth predictability. It is composed mainly of events along the San Andreas just northwest of the Salton Sea, and it is less clear why the models perform poorly here. In contrast, all 12 models yield p < 0.01 in region 48 (southeast of Salton Sea) with model M 2.2 ($M_{\rm L}$ – $M_{\rm c,2}$), giving the overall maximum R^2 value of 0.33. Similarly, all 12 models yield p < 0.01 for the downsampled group of 1000 spatially balanced earthquakes.

Row	Model	Data Grouping										
		a8	с8	18	28	38	48	58	68	78	88	DS
1	M2.1: $m_0 + m_1[M_L - M_{c,1}]$	0.64	2.56	0.90	1.27	1.18	26.39	7.88	3.21	1.90	8.88	5.41
2	M2.2: $m_0 + m_1 [M_L - M_{c,2}]$	1.25	2.64	3.35	3.67	3.55	33.06	10.39	7.15	5.01	11.75	9.95
3	M2.3: $m_0 + m_1[M_{w,P} - M_{c,1}]$	6.18	0.14	0.03	0.23	0.83	19.79	1.23	1.10	3.38	8.55	2.10
4	M2.4: $m_0 + m_1[M_{w,P} - M_{c,2}]$	6.15	0.01	1.34	1.21	1.44	13.67	0.10	0.98	3.78	9.02	5.34
5	M2.5: $m_0 + m_1[M_{w,S} - M_{c,1}]$	1.00	0.79	0.00	0.16	0.00	13.87	0.40	4.96	0.41	10.83	1.33
6	M2.6: $m_0 + m_1[M_{w,S} - M_{c,2}]$	2.17	0.88	2.31	1.29	0.32	10.78	0.52	5.17	1.50	13.29	4.82
7	M2.7: $m_0 + m_1[\log(M_{0,P}) + 3\log(f_{c,P})]$	1.11	0.23	9.28	2.24	1.20	9.15	16.24	2.68	3.62	4.12	6.07
8	M2.8: $m_0 + m_1[\log(M_{0,S}) + 3\log(f_{c,S})]$	0.93	0.00	9.78	1.84	1.60	7.15	18.17	6.70	0.13	0.48	5.23
9	M2.9: $m_0 + m_1 \log(Rg/Sg)$	1.79	1.39	7.58	2.68	1.38	13.88	24.46	4.72	3.29	8.65	11.92
10	M2.10: $m_0 + m_1(Pg_1/Sg_1)$	0.16	1.15	7.12	4.30	0.96	6.98	19.94	3.06	0.07	10.22	9.12
11	M2.11: $m_0 + m_1(Pg_2/Sg_2)$	0.60	0.00	4.46	2.89	0.59	10.52	8.90	2.48	0.22	6.40	4.37
12	M2.12: $m_0 + m_1(Pg_3/Sg_3)$	0.79	0.22	1.73	0.17	0.20	10.21	3.66	3.07	0.45	4.41	0.50
13	M3.1: $m_0 + m_1 M_L + m_2 M_{c,1}$	3.95	2.68	1.14	3.77	1.35	31.82	11.02	6.30	6.83	20.60	11.74
14	M3.2: $m_0 + m_1 M_L + m_2 M_{c,2}$	4.37	3.05	3.77	6.06	3.88	34.10	12.72	10.18	9.93	19.74	14.06
15	M3.3: $m_0 + m_1 M_{w,P} + m_2 M_{c,1}$	6.27	1.30	0.03	0.70	1.67	21.13	4.92	1.20	3.64	8.55	2.99
16	M3.4: $m_0 + m_1 M_{w,P} + m_2 M_{c,2}$	6.47	1.41	1.54	1.38	3.47	13.70	3.38	1.00	3.78	9.75	5.37
17	M3.5: $m_0 + m_1 M_{\text{w,S}} + m_2 M_{\text{c,1}}$	2.26	1.70	0.04	2.10	0.02	17.28	0.43	5.04	3.09	12.26	3.13
18	M3.6: $m_0 + m_1 M_{\text{w,S}} + m_2 M_{\text{c,2}}$	2.84	2.33	2.32	2.67	0.49	11.02	0.53	5.28	3.14	13.32	5.47
19	M3.7: $m_0 + m_1 \log(M_{0,P}) + m_2 \log(f_{c,P})$	2.59	1.66	10.05	4.22	1.27	14.19	16.25	4.04	5.91	7.19	7.50
20	M3.8: $m_0 + m_1 \log(M_{0,S}) + m_2 \log(f_{c,S})$	3.29	1.25	11.38	6.79	1.63	16.96	20.08	8.28	4.03	4.13	8.33
21	M7.1: $m_0 + m_1 M_{\rm L} + m_2 M_{\rm c,2} + m_3 M_{\rm w,P} + m_4 f_{\rm c,P} + m_5 \log(Rg/Sg) + m_6 (Pg_1/Sg_1)$	17.02	8.94	27.29	16.73	9.77	37.17	53.62	23.49	19.05	38.61	24.27
22	M7.2: $m_0 + m_1 M_{\rm L} + m_2 M_{\rm c,2} + m_3 M_{\rm w,S} + m_4 f_{\rm c,S} + m_5 \log(Rg/Sg) + m_6 (Pg_1/Sg_1)$	14.00	8.99	27.93	16.41	10.39	35.15	52.62	27.96	22.76	42.31	23.56
23	$\begin{aligned} \mathbf{M9.1:} \ m_0 + m_1 M_{\mathrm{L}} + m_2 M_{\mathrm{c},2} + m_3 M_{\mathrm{w},P} + \\ m_4 M_{\mathrm{w},S} + m_5 \mathrm{log}(f_{\mathrm{c},P}) + m_6 \mathrm{log}(f_{\mathrm{c},S}) + \\ m_7 \mathrm{log}(Rg/Sg) + m_8 (Pg_1/Sg_1) \end{aligned}$	21.45	11.29	31.16	19.33	10.71	37.94	58.58	25.40	25.37	40.48	24.82

We present depth predictions for the four highest performing models (M 2.2, 2.7, 2.9, and 2.10) in Figure 10. There is a significant variation from region to region, but it is mostly in the constant offset term (m_0) , and the slopes (m_1) are more consistent. The outlier predictions for each model tend to be for regions a8, c8, and 38, which generally have the poorest model fits (Fig. S16). The predictions for the regionally balanced DS data group are shown with red lines in Figure 10, and they generally plot in the middle of the predictions for the individual regions. The values of the slopes are noticeably different than the inverse of slopes determined from regressions shown earlier (e.g., Fig. 3), in which depth was treated as the independent variable. This is owing to the relatively low correlations and the fact that there is significant uncertainty in both the variables. Orthogonal regression that accounts for uncertainties in both the variables would be more appropriate for creating optimal empirical relationships (e.g., Thingbaijam et al., 2017), but in this study we are primarily focused on the significance of parameter correlations.

Bilinear regression of modified waveform features

Depth predictability can be increased by broadening the twoparameter models into more flexible three-parameter models

Figure 9. Results of linear regressions using waveform features as predictor variables for focal depth. The value in each cell indicates $100\% \times R^2$, and green is used to indicate that the correlation is significant with p < 0.01. Descriptions of each of the 23 model types are given in the first column, with m_i indicating a model parameter. Descriptions of each dataset are given across the top row, with DS representing a regionally balanced dataset composed of 100 events from each of the ten geographical regions (a8, c8, 18, ...) shown in Figure 2.

(models M 3.1, 3.2, ..., 3.8 in rows 13–20 of Fig. 9). For instance, model M 2.1

Depth =
$$m_0 + m_1(M_L - M_{c,1})$$
, (5)

is expanded to model M 3.1 as

Depth =
$$m_0 + m_1 M_L + m_2 M_{c,1}$$
, (6)

and bilinear regression is performed to estimate m_0 , m_1 , and m_2 . This expanded parametrization is applied to all six of the differential magnitude models. We also add an extra parameter to the relative frequency indicator models to allow for relationships more flexible than $M_0 \sim f_{\rm c}^{-3}$ (i.e., we treat the

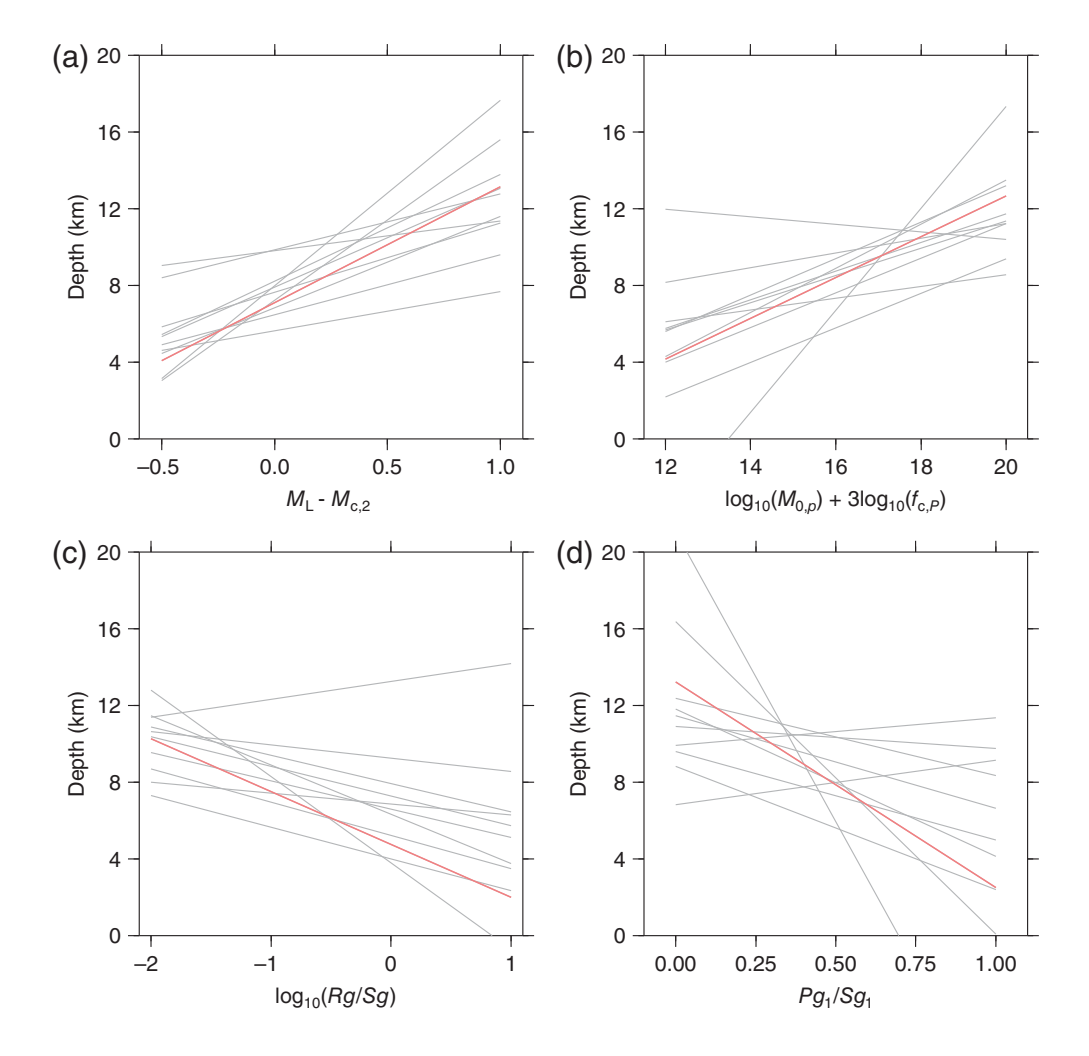


Figure 10. Optimal linear models for (a) $M_L - M_{c,2}$, (b) $\log_{10}(M_{0,P}) + 3 \log_{10}(f_{c,P})$, (c) $\log_{10}(Rg/Sg)$, and (d) Pg, 1/Sg, 1, which are calculated at 3–5 Hz. In each panel, the gray lines correspond to different region data groupings (a8, c8, 18, ...), and the red line corresponds to the regional averaged data grouping DS.

corner frequency exponent as a model parameter as in Kanamori and Rivera, 2004) giving a total of eight threeparameter models. R^2 values for the 88 corresponding bilinear regressions are shown in Figure 9 (rows 13-20). The overall range (0.00-0.34) is like that for the two-parameter models, but the average performance is much better, with 73% of the models having p < 0.01. Average R^2 values are also significantly higher compared to the two-parameter models. For example, average R² grows from 0.083 (M 2.2) to 0.111 (M 3.2) for models involving M_L and $M_{c,2}$. Region-to-region variability in model performance is comparable to that of the two-parameter results: regions c8 and 38 remain problematic, fits for regions a8 and 78 are much improved, and regions 48, 88, and DS retain strong depth predictability. We again find better performance with $M_{c,2}$ instead of $M_{c,1}$, with models M 3.2, 3.4, and 3.6 outperforming models M 3.1, 3.3, and 3.5, respectively. The models based on P- and S-wave derived source spectra (M 3.7 and 3.8) perform similarly.

We expect $m_1 > 0$ and $m_2 < 0$ for the six differential magnitude models (M 3.1-3.6), because this relationship implies a relative decrease in coda wave generation as depth increases. Figure 11a shows the distribution of optimal (m_1, m_2) pairs for the 66 bilinear regressions involving differential magnitudes. Nearly all the points plot in the expected quadrant and roughly follow the $m_2 = -m_1$ trend that line was implicitly assumed in the two parameter models. The most significant models, with p < 0.01, tend to have m_2 slightly less than $-m_1$, implying an upweighting of the coda duration magnitude relative to the reference magnitude, be it $M_{\rm w}$ or $M_{\rm L}$. For instance, the optimal version of model M 2.2 for the DS data group is

Depth =
$$7.60 + 4.45(M_L - M_{c2})$$
, (7)

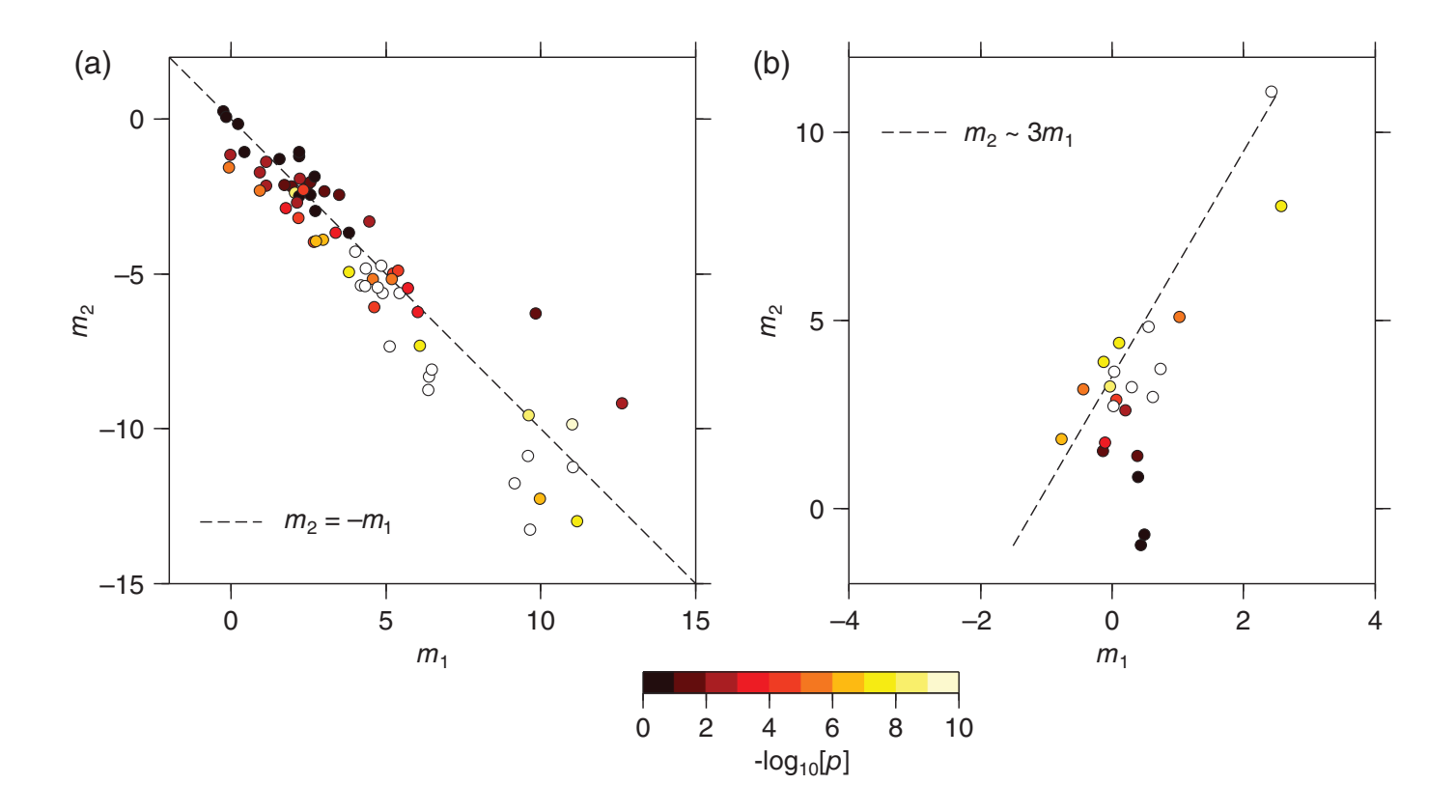
with $R^2 = 0.100$, whereas the optimal version of model M 3.2 for the DS data group is

Depth =
$$10.66 + 6.48M_L - 8.10M_{c,2}$$
, (8)

with $R^2 = 0.140$. In a similar way, we expect that earthquakes with larger moments will have smaller corner frequencies. Assuming constant stress drop and the source model of Eshelby (1957) we expect that $M_0 \sim f_c^{-3}$, which is implicit in models **M** 2.6 and 2.7, and so for the corresponding three-parameter models **M** 3.6 and 3.7, the expectation is that $m_2 \sim 3m_1$. In Figure 11b, we show that the optimal (m_1, m_2) pairs across all the data regions roughly follow that trend if the low-significance pairs with p > 0.01 are ignored.

Multilinear regression of combined waveform features

We next consider three higher-order models that combine waveform features. In model **M** 7.1, we combine M_L , $\log_{10}(Rg/Sg)$, $M_{0:P}$, and $f_{c:P}$, with the better of the two coda duration magnitudes ($M_{c:2}$), and the best of the three Pg/Sg amplitude ratios (3–5 Hz), to create a seven-parameter model.



In **M** 7.2, we exchange $M_{0.S}$ and $f_{c.S}$ for $M_{0.P}$ and $f_{c.P}$. In the nine-parameter model, **M** 9.1, we include all four parameters inferred from source spectra with the other four features from **M** 7.1. R^2 values for the 33 corresponding regressions are reported in Figure 9 (rows 21–23). They are in the range of 0.089–0.586, much higher than the lower order models, and all but three models (94%) yield p < 0.01. The p-values shown in Figure S15 demonstrate that the improved R^2 values for the higher order models are not simply due to the increase in the number of model parameters but represent genuinely better models.

The same region-to-region variability mostly holds for the higher order models, although region 58 becomes the most depth predictable with R^2 values of 0.52–0.58, equivalent to correlation coefficients of 0.72-0.76 between the observed and predicted depths. We speculate that depths in region 58 are so well predicted because it has a relatively small number of data, a small geographic footprint, which implies similar source-receiver paths, and a broad range of depths. The lowest p-values are found for the N = 1,000, regionally balanced, DS data group that has R^2 of 0.20–0.23. For the nine-parameter model M 9.1, depths in all the data groupings except c8 can be fit with p < 0.01. Because M 9.1 also has a higher region averaged R^2 than M 7.1 and 7.2 (0.279 vs. 0.251 and 0.256), we select it as our preferred model parameterization. We experimented with an 11-parameter model that added the two higher frequency Pg/Sg amplitude ratios as predictor variables but found that it did not produce significantly better fits than M 9.1 across all the regions.

Figure 11. (a) Optimal model parameters for models of the type: depth = $m_0 + m_1 M_{\rm w}/M_{\rm L} - m_2 M_{\rm c}$ (**M** 3.1–3.6). (b) Optimal model parameters for models of the type: depth = $m_0 + m_1 \log_{10}(M_0) + m_2 \log_{10}(f_{\rm c})$ (**M** 3.7, 3.8). The color scale indicates $-\log_{10}$ of the p-value. The dark red to black colors have p < 0.01 (i.e., $-\log_{10}(p) < 2$) and represent relatively poor model fits.

In analogy with evaluation methods used for Septor and other deep learning studies, we can treat the DS data group as our training set and evaluate the optimal M 9.1 model parameters on a test set of events that were not used in the regression. There are an additional 2338 earthquakes spread across 10 geographical regions (not including b8), for which all 12 features were successfully calculated. Using M 9.1 to predict depths for these test events gives an R^2 of 0.217, compared to an R^2 of 0.222 for the training events. We further explore the regional variability of the M 9.1 parameters by performing a drop-one-out test. For each region, we find optimal M 9.1 parameters using data from the nine other regions and then use this model to predict depths in the omitted region. Combining results from the 10 drop-out tests gives an R^2 of 0.137—a reduction of ~37% from the original training set. This is a less drastic reduction compared to the results of a similar drop-one-out test used with Septor, which resulted in a >99% reduction in R^2 (Siddiquee et al., 2022), but still implies that the strong geological and tectonic heterogeneity across southern California substantially influences how focal depth is imprinted on waveforms.

DISCUSSION

"Blue Shift" of source spectra with increased focal depth

Our finding that seismic radiation produced by small earthquakes in southern California tends to become enriched in high frequencies as focal depth increases (Fig. 5, Fig. S11) is consistent with previous studies across a broad range of environments. This phenomenon was observed on the Parkfield segment of the San Andreas fault in central California by Allmann and Shearer (2007), who found that apparent stress drop increased by about one order of magnitude over the depth range of 0-4 km without correcting for the increase in shear velocity with depth. Mousavi et al. (2016) studied two populations of well-located microearthquakes in Louisiana: one clustered at depths < 300 m and the other with depths of 1000-2000 m. They used machine learning to identify which waveform features were most effective at separating the two groups and found that the spectral centroid was arguably the most important feature, with the deeper events enriched in high frequencies. During megathrust earthquakes at subduction zones, it is recognized that deeper patches of the fault plane (≥30 km) preferentially radiate higher frequency energy because of a combination of changing stress conditions and material properties (Lay et al., 2012). Conversely, anomalously tsunamigenic earthquakes that rupture primarily within soft sediments at very shallow depths are depleted in high-frequency energy (e.g., Ye et al., 2016). Most recently, Cui et al. (2023) analyzed 3675 source models from a global database of large earthquakes at depths of 0-700 km (Vallee and Douet, 2016) and showed how the increase in rigidity with depth throughout the crust and upper mantle can explain higher frequency content-higher corner frequencies for equivalent moments—as centroid depth increases.

Decreased coda wave generation with increased focal depth

Our finding that M_L - M_c increases with focal depth for small earthquakes recorded at local distances in southern California is consistent with analogous studies in Utah, Yellowstone, the central United States, and Italy (Holt et al., 2019). The increase implies that M_c is anomalously high at shallow depths and systematically decreases as focal depth increases. This interpretation is supported by the new results presented here that $M_{\rm w}$ - $M_{\rm c}$ also increases with depth in southern California, suggesting that depth-dependent changes to M_L are not driving the M_L - M_c changes. Decreased coda wave generation with focal depth is also supported by the decrease in *Rg/Sg* amplitude ratios observed here (Fig. 7). We found little direct evidence for Rg in the spectrograms computed in southern California (Fig. S14) and so interpret the Rg amplitude measurement as indicative of Sg coda energy. Therefore, decreased Rg/Sg ratios with depth are interpreted as decreased Sg,coda/Sg,direct ratios with depth. The numerator is measured at frequencies of 0.5–2.0 Hz, and the denominator is measured at 0.5–8.0 Hz, hence the ratio also likely decreases with depth because of the high-frequency enrichment discussed previously.

There are several mechanisms that may explain stronger coda waves for very shallow seismic events, although their relative importance is poorly known. It has been suggested that elastic scattering of Rg into Lg/Sg is a viable mechanism for creating shear waves from explosions (e.g., Myers et al., 1999). The scattering could be accomplished by topography or other near-surface heterogeneity and would explain the relatively high attenuation of Rg with distance. Because Rg excitation decreases with focal depth, we would expect any related scattered energy in the coda to decrease with focal depth as well (Murphy et al., 2009). Besides topography, stochastic volumetric heterogeneities related to the geologic fabric may enhance scattering (e.g., Scalise et al., 2020), and it is reasonable to expect a higher concentration of stochastic heterogeneity at shallower depths (e.g., Isken and Mooney, 2017). A shallow low-velocity layer can also help trap energy and create extra coda waves, especially for sources that nucleate within the layer (e.g., Imperatori and Mai, 2013). Finally, deterministic 3D structures such as sedimentary basins can create extra-long duration coda waves for especially shallow earthquakes (e.g., Lai et al., 2020).

Decreased P/S ratios with increased depth

We find evidence that *Pg/Sg* amplitude ratios decrease with focal depth in most of our geographical regions (Figs. 6, 9, and Figs. S12, S13). The decrease is not as severe as with *Rg/Sg* amplitude ratios but is generally statistically significant. For instance, in regions 18 and 48 the *Pg/Sg* amplitude ratios decrease by about 50% over the depth range of 1–20 km, depending on the frequency band. The reductions are slightly more significant at lower frequencies (3–5 Hz) than at middle (5–6.5 Hz) or higher frequencies (6.5–8 Hz) (Fig. 9, Fig. S15). As expected, depth averaged *Pg/Sg* values increase with frequency, with means of 0.38, 0.44, and 0.53.

Relatively few studies have evaluated the dependence of P/S amplitude ratios on earthquake focal depth. Using a set of 50 crustal earthquakes in southern Nevada that were recorded regionally, Goldstein (1995) observed that average Pn/Lg spectral amplitude ratios were about three times higher for shallow earthquakes (depth ~ 1.5 km) relative to "normal depth" (depth ~ 15 km) earthquakes. Using a similar dataset, Walter et al. (1995) found comparable results though with a weaker overall separation and significant interstation variability; however, neither study was focused on potential depth dependence of P/S amplitude ratios. In contrast, Zhang et al. (2002) explicitly examined the dependence of P/S amplitude ratios on focal mechanism and focal depth with the aim of better understanding how scatter in earthquake P/S ratios is controlled by source versus path effects (e.g., Fan and Lay, 1998). They studied vertical component (Pg, Pn)/Lg amplitude ratios at 0.5–10 Hz using

data from hundreds of earthquakes in southern California and the Nevada Test Site that were recorded at regional distances (\sim 100 to 1000 km) in the western United States. They observed some coherent trends between focal depth and P/S amplitude ratios, but there was strong regional variation, and they concluded that most of the variance was not deterministically predictable. Similarly, Taylor *et al.* (1989) reported no depth dependence in Pg/Lg amplitude ratios calculated for about 130 western U.S. earthquakes. The clearer trends observed here are probably owing to more accurate depths facilitated by the increased density of seismometers in southern California over the last two decades and advances in absolute and relative source location (Hauksson *et al.*, 2012).

Some previous studies of P/S ratios from explosions have observed the opposite effect, with P/S ratios increasing as depth increases. Taylor et al. (1989) observed a steady decrease in Lg/ Pg (i.e., increase in Pg/Lg) ratios of about a factor of 3 as depth increased from 200 to 800 m for over 200 nuclear explosions detonated at Nevada Test Site and recorded at local-to-regional distances in the western United States. Myers et al. (1999) found that Pg/Sg ratios at 0.7-5 Hz increased with depth for three 25 ton chemical explosions detonated at 50, 300, and 550 m in Kazakhstan, though the ratios were constant with depth at higher frequencies. Most recently, Pyle and Walter (2022) studied Pg/Lg amplitude ratios at distances < 200 km for about 20 chemical explosions detonated near the Nevada Test Site. They found no strong trend between Pg/ Sg and depth, which varied from -2 m to 385 m, or scaled depth of burial, which varied from 0 to 3156 mkt^{-1/3} but did find slightly higher ratios for deeper events on average. They argued that these observations and the earlier Nevada Test Site observations of Taylor et al. (1989) might be explained just as well by differences in material strength as opposed to differences in depth. In any case, the depth regime of all the explosion studies is ~0 to 1 km, whereas the depth regime for our earthquake study is ~1 to 20 km, so different behavior might be expected.

One model that might explain why earthquake P/S amplitude ratios vary with depth has to do with the effect of changes in elastic moduli during faulting. Ben-Zion and Ampuero (2009) proposed that near-fault material damage during an earthquake can act as a secondary source of seismic radiation that has a strong isotropic component and so preferentially enhances P-wave generation. If this effect is significant in southern California and damage preferentially occurs at shallower depth, this model might explain our observations. However, Cheng et al. (2021) examined non-double-couple components of moment tensors for 224 aftershocks of the 2019 M 7.1 Ridgecrest sequence (cluster 18 in this study, Fig. 2) and found no clear dependence on focal depth. A second model that might explain our observations relates to the way Lg is excited by events of different depth (Baker et al., 2004). Those authors report that very shallow events tend to have delayed Lg waves because they preferentially excite shallow low-velocity modes, whereas the depth effect on Pg is more muted. They speculate that Lg energy from shallow events might also be preferentially attenuated by low-Q layers near the surface compared to Pg, which would lead to a general decrease in Pg/Lg amplitude ratios as focal depth increases, matching our observations.

Other waveform features with sensitivity to focal depth

Our exploration of physics-based waveform features that are potentially sensitive to focal depth is not complete, and other possibilities exist for future studies of focal depth predictability. Examples that may be appropriate for our case of small events recorded at local distances include stacks of autocorrelograms (Zhang *et al.*, 2014), *Sn/Lg* amplitude ratios (Wang and Klemperer, 2021), the dominant period of Rayleigh waves (He *et al.*, 2023), and cepstral analysis of *P* coda (Kemerait *et al.*, 2023).

CONCLUSIONS

We calculated magnitudes, source spectra, and phase ratios for ~8000 well-located earthquakes that occurred in southern Californian between 2001 and 2020 with magnitudes of $2 < M_{\rm L} < 4$ and depths of $\sim 1-20$ km. Source–receiver distances were less than 150 km. We identified several waveform features that were significantly sensitive to focal depth. Differential magnitudes of the type $M_{\rm w}/M_{\rm L}$ – $M_{\rm c}$ were positively correlated with focal depth, consistent with decreased coda wave production for deeper earthquakes. Similarly, a simple indicator of relative frequency content, $\Phi \equiv \log_{10}(M_0) + 3\log_{10}(f_c)$, was positively correlated with focal depth, consistent with a "blue shift" toward higher frequency content in deeper earthquakes. Conversely, we found that Rg/Sg spectral amplitude ratios were negatively correlated with focal depth. In general, Rg was poorly observed, and these measurements are more indicative of Sg, coda/Sg,direct amplitude ratios. Thus, their decrease with depth is consistent with our differential magnitude finding that coda wave generation decreases as focal depth increases. We also observed that Pg/Sg spectral amplitude ratios at 3-8 Hz were negatively correlated with focal depth, possibly because of preferential attenuation of Sg energy for shallow earthquakes.

All of these depth-dependent waveform features are useful in discriminating earthquakes from explosions, suggesting that part of their discriminatory power is related to the shallower depths of explosions relative to earthquakes. Results from the upcoming Rock Valley Direct Comparison experiment (Walter et al., 2012; Snelson et al., 2022), in which two single-fired chemical explosions will be detonated within the hypocentral region of an especially shallow 1993 earthquake sequence, should help clarify the extent to which the discriminants reflect differences in source depth versus differences in source mechanisms such as equivalent force models (i.e., double-couple vs. isotropic vs. compensated linear vector dipole).

We used conventional multilinear regression to explore the predictability of focal depth with combinations of waveform features as predictor variables. Our preferred nine-parameter models yielded R^2 values of 0.11–0.59 across 10 subregions and a value of 0.25 on a regionally balanced subset of 1000 earthquakes. Although these R^2 values are somewhat low, they all correspond to p-values \ll 0.01, and the null hypothesis of no correlation can be rejected with extremely high confidence. In terms of variance reduction, our feature-based model performed more poorly than Septor—the deep learning model of Siddiquee et al. (2022)—but seemed more transportable and less overfit. Our feature-based model could likely be improved using approaches more sophisticated than ordinary least squares, such as generalized additive models or Gaussian process regression, or a deep learning approach that combines our physics-based waveform features with neural networks (e.g., Kong et al., 2022).

DATA AND RESOURCES

All the waveform data used here were obtained from the Data Management Center (DMC) of the entity formerly known as Incorporated Research Institutions for Seismology (IRIS) and presently known as Earthscope (https://ds.iris.edu/ds/nodes/dmc/). The earthquake catalog was obtained from the Southern California Earthquake Data Center (SCEDC; https://scedc.caltech.edu/). All websites were last accessed in April 2024. The supplemental material for this article includes 16 figures and related captions.

DECLARATION OF COMPETING INTERESTS

The authors acknowledge that there are no conflicts of interest recorded.

ACKNOWLEDGMENTS

This work was funded by the Air Force Research Laboratory under Award Number FA9453-21-9-0054. The authors thank the Southern California Earthquake Data Center (SCEDC) for making their earthquake catalog available. Egill Hauksson provided advice on interpreting the depths of aftershocks to the 2010 $M_{\rm w}$ 7.2 El Mayor-Cucapah earthquake. Greg Beroza provided advice on interpreting the depths of earthquakes near the Santa Barbara channel. The authors thank Eli Baker for comments on an early draft of the article. The authors thank Tobias Diehl, an anonymous reviewer, and Associate Editor Adrian Oth for important comments and advice during peer review. Sandia National Laboratories (SNL) is a multimission laboratory managed and operated by National Technology and Engineering Solutions of Sandia, LLC, a wholly owned subsidiary of Honeywell International, Inc., for the U.S. Department of Energy's National Nuclear Security Administration under Contract Number DE-NA-0003525. The views expressed in the article do not necessarily represent the views of the U.S. Department of Energy or the U.S. Government.

REFERENCES

Abercrombie, R. E. (1995). Earthquake source scaling relationships from -1 to 5 $M_{\rm L}$ using seismograms recorded at 2.5-km depth, *J. Geophys. Res.* **100**, 24,015–24,036.

- Abercrombie, R. E., D. T. Trugman, P. M. Shearer, X. Chen, J. Zhang, C. N. Pennington, J. L. Hardebeck, T. H. W. Goebel, and C. J. Ruhl (2021). Does earthquake stress drop increase with depth in the crust? *J. Geophys. Res.* **126**, e2021JB022314, doi: 10.1029/2021JB022314.
- Allmann, B. P., and P. M. Shearer (2007). Spatial and temporal stress drop variations in small earthquakes near Parkfield, California, *J. Geophys. Res.* **112,** no. B4, doi: 10.1029/2006JB004395.
- Anderson, D. N., W. R. Walter, D. K. Fagan, T. M. Mercier, and S. R. Taylor (2009). Regional multistation discriminants: Magnitude, distance, and amplitude corrections, and sources of error, *Bull. Seismol. Soc. Am.* 99, 794–808.
- Ataeva, G., Y. Gitterman, and A. Shapira (2017). The ratio between corner frequencies of source spectra of *P* and *S*-waves—A new discriminant between earthquakes and quarry blasts, *J. Seismol.* **21**, 209–220.
- Bachura, M., and T. Fischer (2019). Waveform cross-correlation for differential time measurements: Bias and limitations, *Seismol. Res. Lett.* **90**, 2005–2014.
- Baker, G. E., J. Stevens, and H. Xu (2004). L_g group velocity: A depth discriminant revisited, *Bull. Seismol. Soc. Am.* **94**, 722–739.
- Ben-Zion, Y., and J.-P. Ampuero (2009). Seismic radiation from regions sustaining material damage, *Geophys. J. Int.* **178**, 1351–1356.
- Bowers, D., and N. D. Selby (2009). Forensic seismology and the Comprehensive Nuclear-Test-Ban-Treaty, *Annu. Rev. Earth Planet. Sci.* 37, 209–236.
- Brocher, T. M. (2008). Compressional and shear-wave velocity versus depth relations for common rock types in northern California, *Bull. Seismol. Soc. Am.* **98**, 950–968.
- Brune, J. (1970). Tectonic stress and the spectra of seismic shear waves from earthquakes, *J. Geophys. Res.* **75**, 4997–5009.
- Cheng, Y., X. Wang, Z. Zhan, and Y. Ben-Zion (2021). Isotropic source components of events in the 2019 Ridgecrest, California, earthquake sequence, *Geophys. Res. Lett.* **48**, e2021GL094515, doi: 10.1029/2021GL094515.
- Cui, X., Z. Li, and Y. Hu (2023). Similar seismic moment release process for shallow and deep earthquakes, Nat. Geo. 16, 454–460.
- Deichmann, N. (2017). Theoretical basis for the observed break in M_L/M_w scaling between small and large earthquakes, *Bull. Seismol. Soc. Am.* **107**, 505–520.
- Diehl, T., E. Kissling, M. Herwegh, and S. M. Schmid (2021). Improving absolute hypocenter accuracy with 3D P_g and S_g body-wave inversion procedures and application to earthquakes in the Central Alps region, *J. Geophys. Res.* **126**, e2021JB022155, doi: 10.1029/2021JB022155.
- Douglas, A. (2013). Forensic Seismology and Nuclear Test Bans, Cambridge University Press, Cambridge, United Kingdom, 514 pp.
- Dreger, D. S., and D. V. Helmberger (1993). Determination of source parameters at regional distances with three-component sparse network data, *J. Geophys. Res.* **98**, 8107–8125.
- Edwards, B., B. Allmann, D. Fah, and J. Clinton (2010). Automatic computation of moment magnitudes for small earthquakes and the scaling of local to moment magnitude, *Geophys. J. Int.* **183**, 407–420.
- Eshelby, J. D. (1957). The determination of the elastic field of an ellipsoidal inclusion, and related problems, *Proc. Math. Phys. Sci.* **241**, 376–396.

- Fan, G., and T. Lay (1998). Statistical analysis of irregular wave-guide influences on regional seismic discriminants in China: Additional results for P_n/S_n , P_n/L_g , and P_g/S_n , Bull. Seismol. Soc. Am. 88, 1504–1510.
- Goebel, T. H. W., E. Haukkson, P. M. Shearer, and J. P. Ampuero (2015). Stress-drop heterogeneity within tectonically complex regions: A case study of San Gorgonio Pass, Southern California, *Geophys. J. Int.* 202, 514–528.
- Goldstein, P. (1995). Slopes of *P* to *S*-wave spectral ratios—A broadband regional seismic discriminant and a physical model, *Geophys. Res. Lett.* **22**, 3147–3150.
- Gomberg, J., K. M. Shedlock, and S. W. Roecker (1990). The effect of S-wave arrival times on the accuracy of hypocenter estimation, *Bull. Seismol. Soc. Am.* **80**, 1605–1628.
- Gulia, L., and P. Gasperini (2021). Contamination of frequency-magnitude slope (b-value) by quarry blasts: An example for Italy, *Seismol. Res. Lett.* **92**, 3538–3551.
- Hanks, T. C., and H. Kanamori (1979). A moment magnitude scale, *J. Geophys. Res.* **84**, 2348–2350.
- Hardebeck, J. L., and A. Aron (2009). Earthquake stress drops and inferred fault strength on the Hayward Fault, East San Francisco Bay, California, Bull. Seismol. Soc. Am. 99, 1801–1814.
- Hauksson, E., J. Stock, K. Hutton, W. Yang, J. A. Vidal-Villegas, and H. Kanamori (2011). The 2010 M_w 7.2 El Mayor-Cucapah earthquake sequence, Baja California, Mexico and southernmost California, USA: Active seismotectonics along the Mexican Pacific margin, *Pure Appl. Geophys.* 168, 1255–1277.
- Hauksson, E., W. Yang, and P. M. Shearer (2012). Waveform relocated earthquake catalog for southern California (1981 to June 2011), *Bull. Seismol. Soc. Am.* **102**, 2239–2244.
- He, X., P. Zhang, S. Ni, R. Chu, W. Wu, and K. Zheng (2023). Automatic determination of focal depth with the optimal period of Rayleigh wave amplitude spectra at local distance, *Geophys. J. Int.* 235, 1681–1696.
- He, X., P. Zhang, S. Ni, and W. Zheng (2019). Resolving focal depth in sparse network with local depth phase *sPL*: A case study for the 2011 Mineral, Virginia, earthquake sequence, *Bull. Seismol. Soc. Am.* 109, 745–755.
- Herrmann, R. B., H. Benz, and C. J. Ammon (2011). Monitoring the earthquake source process in North America, *Bull. Seismol. Soc. Am.* **101**, 2609–2625.
- Holt, M. M. (2021). Seismic discrimination of earthquakes and explosions using comparisons of local magnitude (M_L) and coda magnitude (M_C), *Ph.D. Thesis*, University of Utah, 125 pp.
- Holt, J., K. M. Whidden, K. D. Koper, K. L. Pankow, K. Mayeda, J. C. Pechmann, B. Edwards, R. Gök, and W. R. Walter (2021). Toward robust and routine determination of $M_{\rm w}$ for small earthquakes: Application to the 2020 $M_{\rm w}$ 5.7 Magna, Utah, seismic sequence, *Seismol. Res. Lett.* **92**, 725–740.
- Holt, M. M., K. D. Koper, W. Yeck, S. D'Amico, Z. Li, J. M. Hale, and R. Burlacu (2019). On the portability of M_L-M_C as a depth discriminant for small seismic events recorded at local distances, *Bull. Seismol. Soc. Am.* 109, 1661–1673.
- Horasan, G., A. B. Güney, A. Küsmezer, F. Bekler, Z. Ögütçü, and N. Musaoglu (2009). Contamination of seismicity catalogs by quarry blasts: An example from Istanbul and its vicinity, northwestern Turkey, J. Asian Earth Sci. 34, 90–99.

- Hough, S. E. (1997). Empirical Green's function analysis: Taking the next step, J. Geophys. Res. 102, 5369–5384.
- Imperatori, W., and P. M. Mai (2013). Broad-band near-field ground motion simulations in 3-dimensional scattering media, *Geophys. J. Int.* 192, 725–744.
- Isken, M. P., and W. D. Mooney (2017). Relocated hypocenters and structural analysis from waveform modeling of aftershocks from the 2011 Prague, Oklahoma, earthquake sequence, *Bull. Seismol. Soc. Am.* 107, 553–562.
- Jeong, S., B. W. Stump, and H. D. DeShon (2020). Spectral characteristics of ground motion from induced earthquakes in the Fort Worth Basin, Texas, using the generalized inversion technique, *Bull. Seismol. Soc. Am.* 110, 2058–2076.
- Kafka, A. L. (1990). R_g as a depth discriminant for earthquakes and explosions: A case study in New England, *Bull. Seismol. Soc. Am.* **80**, 373–394.
- Kanamori, H., and L. Rivera (2004). Static and dynamic scaling relations for earthquakes and their implications for rupture speed and stress drop, *Bull. Seismol. Soc. Am.* 94, 314–319.
- Kemerait, R. C., I. M. Tibuleac, J. F. Pascual-Amadeo, D. H. Stayt, M. A. Capuano, and M. Thursby (2023). Quality control metrics for cepstral analysis with homomorphic deconvolution, *Bull. Seismol. Soc. Am.* 113, 1806–1819.
- Kemna, K. B., A. Verdecchia, and R. M. Harrington (2021). Spatiotemporal evolution of earthquake static stress drop values in the 2016–2017 central Italy seismic sequence, *J. Geophys. Res.* **126**, e2021JB022566, doi: 10.1029/2021JB022566.
- Kinter, J. A., K. M. Cleveland, C. J. Ammon, and A. Nyblade (2020). Testing a local-distance R_g/S_g discriminant using observations from the Bighorn Region, Wyoming, *Bull. Seismol. Soc. Am.* 111, 727–741.
- Ko, Y., B. Kuo, and S. Hung (2012). Robust determination of earth-quake source parameters and mantle attenuation, *J. Geophys. Res.* **117,** no. B4, doi: 10.1029/2011JB008759.
- Kolaj, M. (2018). Discriminating between low-magnitude shallow earthquakes and road construction blasts near Big Salmon River, New Brunswick, Canada, Seismol. Res. Lett. 89, 1966–1976.
- Kong, Q., R. Wang, W. R. Walter, M. Pyle, K. Koper, and B. Schmandt (2022). Combining deep learning with physics based features in explosion-earthquake discrimination, *Geophys. Res. Lett.* 49, e2022GL098645, doi: 10.1029/2022GL098645.
- Koper, K. D. (2019). The importance of regional seismic networks in monitoring nuclear test-ban treaties, *Seismol. Res. Lett.* **91,** 573–580.
- Koper, K. D., M. M. Holt, J. R. Voyles, R. Burlacu, M. L. Pyle, R. Wang, and B. Schmandt (2021). Discrimination of small earthquakes and buried single-fired chemical explosions at local distances (<150 km) in the western United States from comparison of local magnitude (M_L) and coda duration magnitude (M_C), Bull. Seismol. Soc. Am. 111, 558–570.
- Korrat, I. M., A. Lethy, M. N. El Gabry, H. M. Hussein, and A. S. Othman (2022). Discrimination between small earthquakes and quarry blasts in Egypt using spectral source characteristics, *Pure Appl. Geophys.* 179, 599–618.
- Lai, V. H., R. W. Graves, C. Yu, Z. Zhan, and D. V. Helmberger (2020). Shallow basin structure and attenuation are key to predicting long shaking duration in Los Angeles Basin, J. Geophys. Res. 125, e2020JB019663, doi: 10.1029/2020JB019663.

- Lay, T., H. Kanamori, C. J. Ammon, K. D. Koper, A. R. Hutko, L. Ye, H. Yue, and T. M. Rushing (2012). Depth-varying rupture properties of subduction zone megathrust faults, *J. Geophys. Res.* 117, no. B4, doi: 10.1029/2011JB009133.
- Lee, T., T. Diehl, E. Kissling, and S. Wiemer (2023). New insights into the Rhône-Simplon fault system (Swiss Alps) from a consistent earthquake catalogue covering 35 yr, *Geophys. J. Int.* **232**, 1568–1589.
- Lin, G., P. M. Shearer, and E. Hauksson (2007). Applying a threedimensional velocity model, waveform cross correlation, and cluster analysis to locate southern California seismicity from 1981 to 2005, J. Geophys. Res. 112, no. B12, doi: 10.1029/2007JB004986.
- Ma, S. (2010). Focal depth determination for moderate and small earthquakes by modelling regional depth phases sP_g , sPmP, and sP_n , Bull. Seismol. Soc. Am. 100, 1073–1088.
- Maceira, M., P. S. Blom, J. K. McCarthy, O. E. Marcillo, G. G. Euler, M. L. Begnaud, S. R. Ford, M. E. Pasyanos, G. J. Orris, M. P. Foxe, et al. (2017). Trends in nuclear explosion monitoring research & development—A physics perspective, *Dept. of Energy Technical Rept. LA-UR-17-21274*, 170 pp., doi: 10.2172/1355758.
- Mayeda, K., and W. R. Walter (1996). Moment, energy, stress drop, and source spectra of western United States earthquakes from regional coda envelopes, *J. Geophys. Res.* **101**, 11,195–11,208.
- Mousavi, S. M., S. P. Horton, C. A. Langston, and B. Samei (2016). Seismic features and automatic discrimination of deep and shallow induced-microearthquakes using neural network and logistic regression, *Geophys. J. Int.* 207, 29–46.
- Mueller, C. S. (1985). Source pulse enhancement by deconvolution of an empirical Green's function, *Geophys. Res. Lett.* **12**, 33–36.
- Murphy, K. R., K. Mayeda, and W. R. Walter (2009). L_g -Coda methods applied to Nevada test site events: Spectral peaking and yield estimation, *Bull. Seismol. Soc. Am.* **99**, 441–448.
- Myers, S. C., W. R. Walter, K. Mayeda, and L. Glenn (1999). Observations in support of *Rg* scattering as a source for explosion *S* waves: Regional and local recordings of the 1997 Kazakhstan depth of burial experiment, *Bull. Seismol. Soc. Am.* **89**, 544–549.
- O'Rourke, C. T., and G. E. Baker (2017). A spectrogram-based method of R_g detection for explosion monitoring, *Bull. Seismol. Soc. Am.* **107**, 34–42.
- Oth, A., H. Miyake, and D. Bindi (2017). On the relation of earth-quake stress drop and ground motion variability, *J. Geophys. Res.* **122**, 5474–5492.
- Parolai, S., and A. Oth (2022). On the limitations of spectral source parameter estimation for minor and microearthqaukes, *Bull. Seismol. Soc. Am.* **112**, 2364–2375.
- Pyle, M. L., and W. L. Walter (2022). Exploring the effects of emplacement conditions on explosions *P/S* ratios across local to regional distances, *Seismol. Res. Lett.* **93**, 866–879.
- Renouard, A., A. Maggi, M. Grunberg, C. Doubre, and C. Hibert (2021). Toward false event detection and quarry blast versus earth-quake discrimination in an operational setting using semiautomated machine learning, *Seismol. Res. Lett.* **92**, 3725–3742.
- Richards, P. G., and J. Zavales (1990). Seismic discrimination of nuclear explosions, *Annu. Rev. Earth Planet. Sci.* 18, 257–286.
- Ross, Z. E., B. Idini, Z. Jia, O. L. Stephenson, M. Zhong, X. Wang, Z. Zhan, M. Simons, E. J. Fielding, S.-H. Yun, et al. (2019). Hierarchical interlocked orthogonal faulting in the 2019 Ridgecrest earthquake sequence, *Science* 366, 346–351.

- Scalise, M., A. Pitarka, J. N. Louie, and K. D. Smith (2020). Effect of random 3D correlated velocity perturbations on numerical modeling of ground motion from the source physics experiment, *Bull. Seismol. Soc. Am.* 111, 139–156.
- Shearer, P. M., R. E. Abercrombie, and D. T. Trugman (2022). Improved stress drop estimates for M 1.5 to 4 earthquakes in Southern California from 1996 to 2019, *J. Geophys. Res.* **127**, e2022JB024243, doi: 10.1029/2022JB024243.
- Shearer, P. M., G. A. Prieto, and E. Hauksson (2006). Comprehensive analysis of earthquake source spectra in southern California, *J. Geophys. Res.* **111**, no. B6, doi: 10.1029/2005JB003979.
- Shible, H., F. Hollender, D. Bindi, P. Traversa, A. Oth, B. Edwards, P. Klin, H. Kawase, I. Grendas, P. R. Castro, et al. (2022). GITEC: A generalized inversion technique benchmark, Bull. Seismol. Soc. Am. 112, 850–877.
- Siddiquee, M. A., G. E. Baker, V. M. A. Souza, and A. Mueen (2022).
 Septor: Seismic depth estimation using hierarchical neural networks,
 Proc. of the 28th ACM SIGKDD Conf. on Knowledge Discovery and
 Data Mining, 3889–3897, doi: 10.1145/3534678.3539166.
- Snelson, C. M., C. R. Bradley, W. R. Walter, T. H. Antoun, R. A. Abbott, K. Jones, V. Chipman, and L. Montoya (2022). The Source Physics Experiment (SPE) science plan, version 3.0, Lawrence Livermore Laboratory Technical Report, LLNL-TR-839815, available at https://www.osti.gov/servlets/purl/1887003 (last accessed October 2023).
- Taylor, S. R., M. D. Denny, E. S. Vergino, and R. E. Glaser (1989).
 Regional discrimination between NTS explosions and western
 U.S. earthquakes, *Bull. Seismol. Soc. Am.* 79, 1142–1176.
- Taylor, S. R., A. A. Velasco, H. E. Hartse, W. S. Phillips, W. R. Walter, and A. J. Rodgers (2002). Amplitude corrections for regional seismic discriminants, *Pure Appl. Geophys.* 159, 623–650.
- Thingbaijam, K. K. S., P. M. Mai, and K. Goda (2017). New empirical earthquake source-scaling laws, *Bull. Seismol. Soc. Am.* **107**, 2225–2246.
- Tibi, R., N. Downey, and R. Brogan (2023). Testing and design of discriminants for local seismic events recorded during the Redmond salt mine monitoring experiment, *Bull. Seismol. Soc. Am.* doi: 10.1785/0120230193.
- Tibi, R., K. D. Koper, K. L. Pankow, and C. J. Young (2018). Depth discrimination using R_g -to- S_g spectral amplitude ratios for seismic events in Utah recorded at local distances, *Bull. Seismol. Soc. Am.* **108.** 1366–1368.
- Trugman, D. T. (2020). Stress-drop and source scaling of the 2019 Ridgecrest, California, earthquake sequence, *Bull. Seismol. Soc. Am.* **110**, 1859–1871.
- Trugman, D. T., and P. M. Shearer (2017). Growclust: A hierarchical clustering algorithm for relative earthquake relocation, with application to the Spanish Springs and Sheldon, Nevada, earthquake sequences, *Seismol. Res. Lett.* **88**, 379–391.
- U. S. Department of Energy (2015). United States Nuclear Tests July 1945 Through September 1992, DOE/NV-2019-REV 16, National Nuclear Security Administration Nevada Field Office, 186 pp.
- Vallee, M., and V. A. Douet (2016). A new database of source time functions (STFs) extracted from the SCARDEC method, *Phys. Earth Planet. In.* 257, 149–157.
- Walter, W. R., and S. R. Taylor (2002). A revised magnitude and distance amplitude correction (MDAC2) procedure for regional

- seismic discriminants: Theory and testing at NTS, *Lawrence Livermore National Laboratory Technical Report UCRL-ID-* 146882, Livermore, California.
- Walter, W. R., K. Mayeda, and H. J. Patton (1995). Phase and spectral ratio discrimination between NTS earthquakes and explosions. Part I: Empirical observations, *Bull. Seismol. Soc. Am.* 85, 1050–1067.
- Walter, W. R., M. L. Pyle, S. R. Ford, S. C. Myers, K. D. Smith, C. Snelson, and V. Chipman (2012). Rock Valley Direct Earthquake-Explosion Comparison Experiment (RV-DC): Initial feasibility study, *Lawrence Livermore Laboratory Technical Report*, *LLNL-TR-585672*, https://www.osti.gov/biblio/1053650 (last accessed October 2023).
- Wang, S., and S. L. Klemperer (2021). Love-wave normal modes discriminate between upper-mantle and crustal earthquakes: Simulation and demonstration in Tibet, *Earth Planet. Sci. Lett.* **571,** 117089.
- Wei, S., E. Fielding, S. Leprince, A. Sladen, J.-P. Avouac, D. Helmberger, E. Hauksson, R. Chu, M. Simons, K. Hudnut, et al. (2011). Superficial simplicity of the 2010 El Mayor-Cucapah earthquake of Baja California in Mexico, Nat. Geo. 4, 615–618.
- National Research Council, Policy and Global Affairs, and Committee on Reviewing and Updating Technical Issues Related to the Comprehensive Nuclear Test Ban Treaty (2012). The Comprehensive Nuclear Test Ban Treaty-Technical Issues for the

- *United States*, The National Academies Press, Washington, D. C., 203 pp.
- Ye, L., T. Lay, H. Kanamori, and L. Rivera (2016). Rupture characteristics of major and great ($M_{\rm w} \ge 7.0$) megathrust earthquakes from 1990 to 2015: 1. Source parameter scaling relationships, *J. Geophys. Res.* **121**, 826–844.
- Yuan, J., H. Kao, and J. Yu (2020). Depth-scanning algorithm: Accurate, automatic, and efficient determination of focal depths for local and regional earthquakes, *J. Geophys. Res.* 125, e2020JB019430, doi: 10.1029/2020JB019430.
- Zhang, J., T. Lay, J. Zaslow, and W. R. Walter (2002). Source effects on regional seismic discriminant measurements, *Bull. Seismol. Soc. Am.* **92**, 2926–2945.
- Zhang, M., D. Tian, and L. Wen (2014). A new method for earthquake depth determination: Stacking multiple-station autocorrelograms, *Geophys. J. Int.* 197, 1107–1116.
- Zollo, A., A. Orefice, and V. Convertito (2014). Source parameter scaling and radiation efficiency of microearthquakes along the Irpinia fault zone in southern Apennines, Italy, J. Geophys. Res. 119, 3256–3275.

Manuscript received 7 December 2023 Published online 7 May 2024